Warp-Field Architecture Based on Structured Casimir-Polder Interactions in BEC-Layered Cavities

Introduction

This work presents a theoretical framework for a propulsion concept based on structured Casimir-Polder interactions within confined Bose-Einstein condensate (BEC) systems. The approach explores the possibility of engineering spatially distributed force fields through controlled phase coherence, nanophotonic coupling, and layered compensation mechanisms.

The proposed configuration aims to generate controlled gradients of effective potential within a bounded region of space. While not constituting a direct manipulation of space-time geometry, such gradients may provide a platform for investigating indirect mechanisms of force redistribution and field compensation in advanced propulsion systems.

The motivation for this study arises from the fundamental relation between energy, mass, and space-time curvature as described by general relativity. Conventional approaches to metric engineering require energy densities far beyond current technological capabilities. This work therefore focuses on alternative strategies based on structured fields and collective quantum effects, which may allow localized control of force distributions without requiring macroscopic space–time curvature.

In this context, the concept of a closed compensation field is introduced as a means of reducing the net interaction between the propulsion system and the surrounding environment. Such a configuration may enable internal field structuring and controlled gradients while minimizing external perturbations.

The framework further considers the implications of non-uniform potential distributions for onboard conditions, including effective gravity gradients and potential time dilation effects although no quantitative relativistic treatment is developed in the present work. These aspects are analyzed qualitatively within the scope of general relativity, with emphasis on the limitations and uncertainties associated with such configurations.

Although highly speculative, the proposed approach is conceptually linked to experimentally accessible platforms, including BEC systems, Casimir-Polder interactions, and nanophotonic structures. The paper outlines the theoretical basis of the model, proposes a sensing and control architecture, and identifies key challenges for potential experimental validation.

Before quantitative estimates of energy requirements can be meaningfully addressed, it is necessary to establish the underlying physical principles and operational model of the proposed system. The present work is therefore focused on the formulation and analysis of this conceptual framework.

Abstract

This work proposes a conceptual model of a propulsion system based on a dynamically modulated warp-bubble-like spacetime configuration. To provide an

intuitive picture, one may consider the effect of the warp core on spacetime geometry as analogous to a localized deformation of an elastic medium.

A dense fiber-optic waveguide beam with continuous photon pulses can be considered as such a core. Electromagnetic radiation contributes to spacetime curvature through its energy-momentum tensor, as described by the Einstein field equations:

$$G_{\mu\nu} = \frac{8\pi G}{c^4} T_{\mu\nu}$$ [1, pp. 151-157], [2, pp. 72-78].

In particular, it is well established that even a beam of light generates a gravitational field [3, pp. 326-329] [4, pp. 602–615], [5, pp. 163-174].

In this context, the energy density associated with a high-intensity laser field can be interpreted as a localized contribution to the effective curvature of spacetime, although such effects are typically extremely small in conventional regimes.

In this analogy, the space-time metric for the compensation field surrounding the warp core varies in a limited area, remaining asymptotically flat outside the system. The engineering task is therefore to construct a field configuration that restores the external region to a near-flat (zero-curvature) state, while maintaining a controlled and spatially uniform deformation within the interior region.

In the standard Alcubierre-type geometry [6, pp. L73–L77], the spacetime distortion can be interpreted as having regions of positive and negative effective curvature relative to the background metric. In particular, the extremal regions of the configuration may be described as having equal magnitude and opposite sign with respect to deviations from the background spacetime.

In the present approach, we instead consider a modified configuration in which the effective gravitational potential does not assume negative values relative to the chosen reference level. This can be interpreted as a shifted potential baseline, where the minimum of the field corresponds to a value comparable to the average gravitational potential in the surrounding region.

Furthermore, by considering a symmetric transformation of the field configuration - such as rotations about orthogonal axes - the spatial distribution of the deformation can be arranged such that inward- and outward-directed gradients are balanced in a controlled manner. In this framework, the lowest potential region is constrained to remain close to the mean background level, thereby avoiding large negative excursions while preserving the overall structure of the warp-like deformation.

In the Alcubierre-type spacetime, both the interior of the bubble and the asymptotic exterior region can be chosen to be locally flat, while the spacetime curvature is concentrated in a thin transition layer (the bubble wall, Figure 1). Therefore, the deformation is not characterized by a global gravitational potential minimum inside the bubble, but rather by a localized modification of the metric in the wall region.

In an effective description, one may associate the interior of the bubble with a region of approximately uniform effective potential, while the exterior corresponds to the background level. However, the physically relevant gradients are localized in the bubble wall, where the spacetime deformation is concentrated.

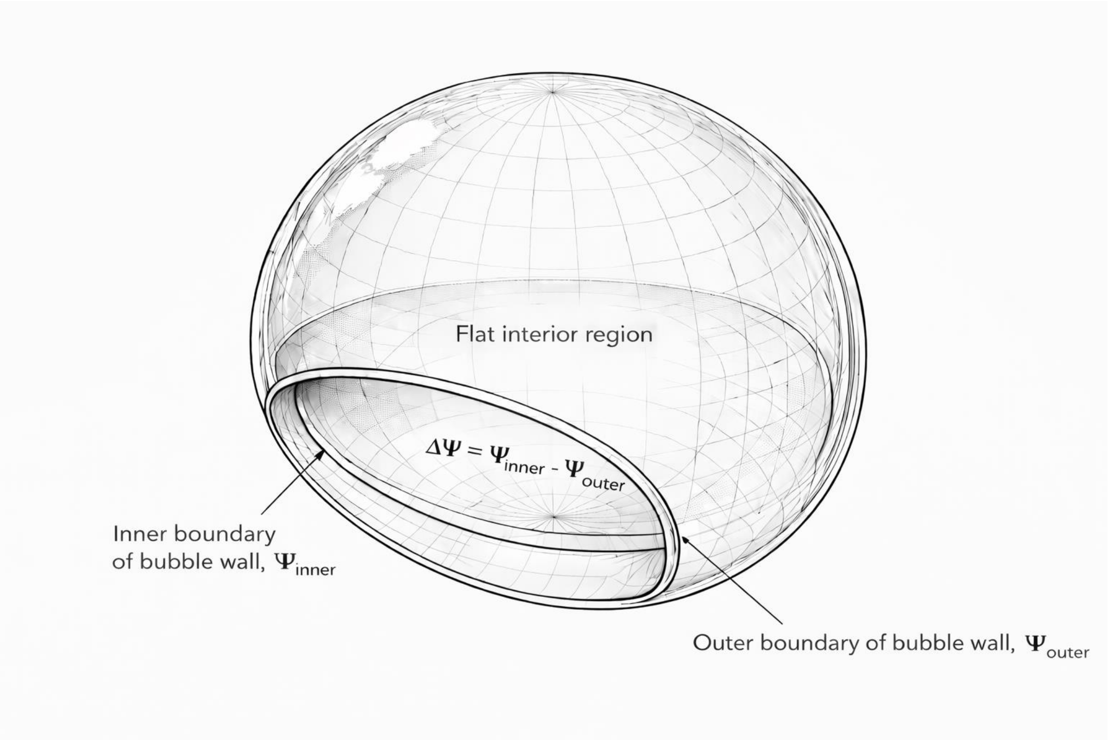

Figure 1.

As an effective engineering estimate, the energy of the warp core can be related to the energy imbalance across the working volume of the bubble wall, as an effective energy-balance estimate:

$$E_{core} \sim E_{field},$$

$$E_{core} \sim \int_{Vwall} \Delta\rho_{eff} \cdot dV,$$

Where:

E_{core} - energy of warp core;

E_{field} - energy of warp compensation field;

V_{wall} - the volume of the working area of the bubble thickness;

$\Delta\rho_{eff} = |\rho_{inner} - \rho_{outer}|$ - effective difference in vacuum energy density between the inner and outer sides of the compensation field;

ρ - effective vacuum-energy density.

This relation is adopted as a design assumption rather than a result derived from first principles.

If the energy of the warp core is greater than the compensation field's, the membrane may bend too much, causing an imbalance. If the warp core energy is too low, the compensation field will not be sufficiently stabilized - this effect will be further discussed in more detail.

Maintaining energy equality is crucial for achieving balance and minimizing interference in space while maximizing efficiency.

Drive Engineering Concept

1.Warp Core

A pulsed-laser system may be employed as the primary energy source, generating synchronized high-energy pulses distributed through a network of fiber-optic channels arranged within a compact, approximately spherical volume.

The architecture is based on a set of $6^{x}n$ optical paths, grouped into three subsystems of $2^{x}n$ channels each. These subsystems operate with relative phase shifts of $2\pi/3$, forming a three-phase modulation scheme.

Within each subsystem, the $2^{x}n$ channels are further divided into two equal subsets of n paths. A relative temporal offset of $\tau/2$ is introduced between these subsets, while the pulse duration is τ and the idle interval is $2^{x}\tau$.

This paired three-phase configuration ensures that the total energy distribution within the core remains approximately uniform, even in the presence of small fluctuations in pulse duration or timing. The resulting redundancy and phase interleaving improve the stability and smoothness of the effective energy delivery.

Since the six transport channels are arranged as three phase-interleaved pairs, only two channels contribute simultaneously to the aggregate optical power flow. The resulting combined duty factor is therefore:

$$D_{tot} = 3\nu\tau,$$

where:
ν is the pulse repetition frequency;
τ is the pulse duration.

The system is designed such that $D_{tot} = 1/3$, allowing the aggregate optical power delivery to approximate a quasi-continuous energy flow at the system level, despite each individual channel operating in a pulsed regime.

This configuration also distributes thermal loading across multiple phase-shifted channels. Because the instantaneous energy delivery is shared among the interleaved waveguides, the peak local power in any single fiber is reduced relative to an equivalent single-channel configuration, mitigating overheating, nonlinear optical damage, and waveguide instability. In this sense, phase interleaving serves simultaneously as a mechanism of energy smoothing and thermal management consistent with phase-interleaved power-distribution and thermal-load-management concepts used in high-power fiber systems [7, pp. 567–577].

2. Warp Compensation Field

To create such a form of distortion (the bubble wall, Figure 1), it makes sense to refer to the results of laboratory experiments:

1. Theoretical and experimental studies associated with White et al. (2021). It has been observed that quantum particles in identical quantum states at very small distances from each other are affected by the Casimir force [8];

2. An experiment with a quantum mirror conducted by scientists from the Max Planck Institute of Quantum Optics [9]. This work shows how an atomic cloud or ensemble can be held by quantum fields so that the atoms in the BEC form quasi-quantum fields.

The Casimir effect describes the change in vacuum fluctuations caused by the imposition of boundary conditions. This can be expressed as:

$$F_{Cas} = -(\pi^2 \hbar c A)/(240 d^4),$$

where:
F_{Cas} is the Casimir force;
$\hbar$ is the reduced Planck constant;
c is the velocity of light;
d is the distance between the plates;
A is the area of the plates.

Approximate formula for two atoms or particles (Casimir-Polder effect): the Casimir-Polder formula is used for two neutral polarizable particles located at a distance r. For distances less than $r \sim c/\omega_0$ ($r \approx 100$ nm), a non-retarded formula is used; for distances greater than this value, a retarded formula is used:

$$F_{n\text{-}ret}(\delta) = -(9\hbar/2\delta^7) \cdot \alpha^2(0)\omega_0 \; [10],$$

$$F_{ret}(\delta) = -(161\hbar \cdot c \cdot \alpha(\omega_0)^2)/(4\pi \cdot \delta^8) \; [10];$$

where:
$\alpha(0)$ is the polarizability coefficient of neutral atom, the unit dimension of the coefficient used in this formula is m^3:
$\alpha(0) \approx 4.73 \times 10^{-29}\ m^3$;
r is the distance between atoms;
$\hbar \approx 1.05 \times 10^{-34}$ J·sec, - reduced Planck constant;
ω_0 - atomic transition frequency;
δ is the distance between atoms.

The formula using polarizability in bulk form is most often used in BEC and condensed gas problems [11], [12]. The force decreases as $1/r^7$ - $1/r^8$, which is typical for long-range vacuum fluctuations.

According to theoretical calculations by Harold White and his colleagues (2021), certain microstructures of Casimir cavities are capable of creating vacuum energy distributions similar to the warp field metric described by Alcubierre. In particular, geometries with distances between elements of the order of tens of micrometers (less than ~10 µm) can induce local fluctuations in vacuum energy, producing vacuum-energy distributions qualitatively resembling certain features of warp-metric energy profiles.

The Casimir-Polder interaction arises between polarizable atoms or between an atom and a structured surface and is fundamentally associated with the separation axis of the interacting system. However, the resulting modification of vacuum fluctuations is not necessarily restricted to this interaction axis alone.

In asymmetric or structured cavity configurations, boundary conditions may induce anisotropic redistribution of vacuum modes in directions determined by the cavity geometry and external photonic excitation. Similar geometry-dependent mode structuring effects are widely encountered in cavity quantum electrodynamics and coherent photonic systems [13, pp. 3-5].

As discussed qualitatively in White et al. (2021), structured Casimir geometries may produce directional stress-energy asymmetries associated with cavity-induced vacuum-mode structuring rather than solely with the direct interaction line between particles.

In the present model, a photonic correction field oriented transverse to the primary atom-atom interaction axis is introduced as a mechanism for controlled anisotropic modulation of the effective vacuum-energy distribution (Figure 2).

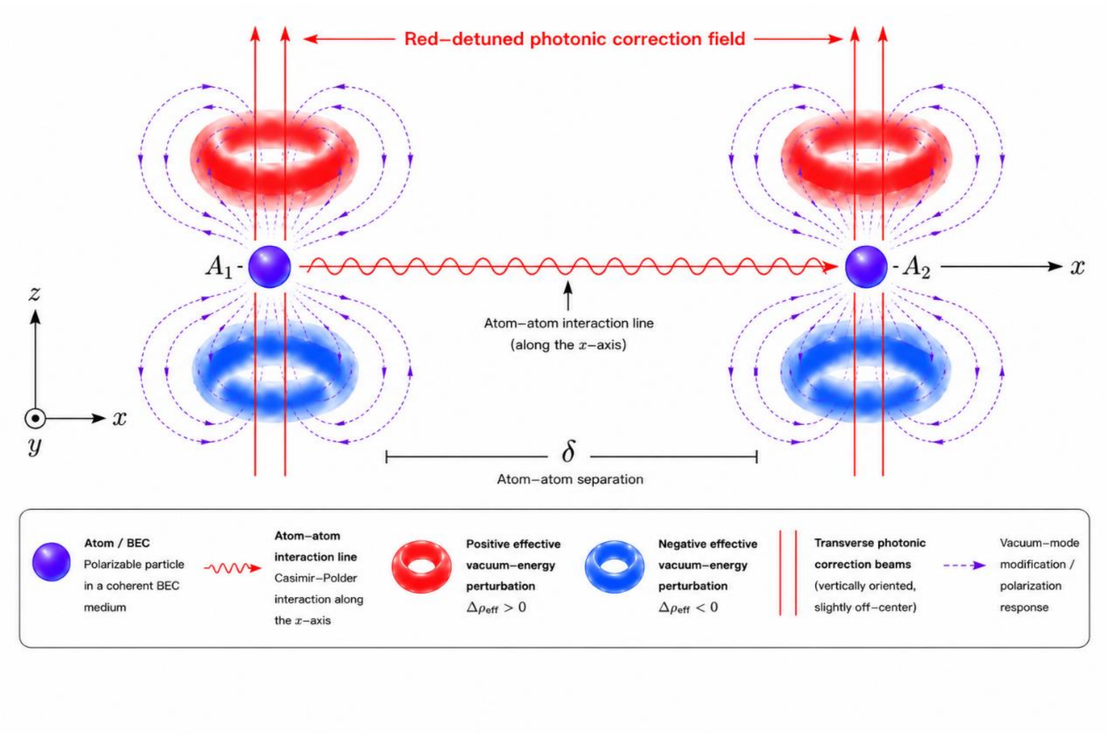

Figure 2. Conceptual schematic of a Casimir-Polder interaction pair aligned along the x-axis with transverse photonic correction along the z-axis.

The cavity geometry and transverse photonic dressing together define a preferred orientation of the resulting effective vacuum-energy perturbation, phenomenologically represented as a gradient directed predominantly along the cavity normal. Analogous orientation-dependent collective effects are commonly observed in optical lattice and coherent quantum-gas systems, where the geometry and angle of external photonic excitation influence anisotropic confinement and phase ordering [14, pp. 24-25].

Such transverse modulation is further assumed to provide an additional degree of control over the coherence, stability, and dynamic tuning of the compensation field, analogous to controllable anisotropic effects observed in optical-lattice systems [14, pp. 24-26], under nonstationary operating conditions involving temporal variations of the effective field energy (Figure 3).

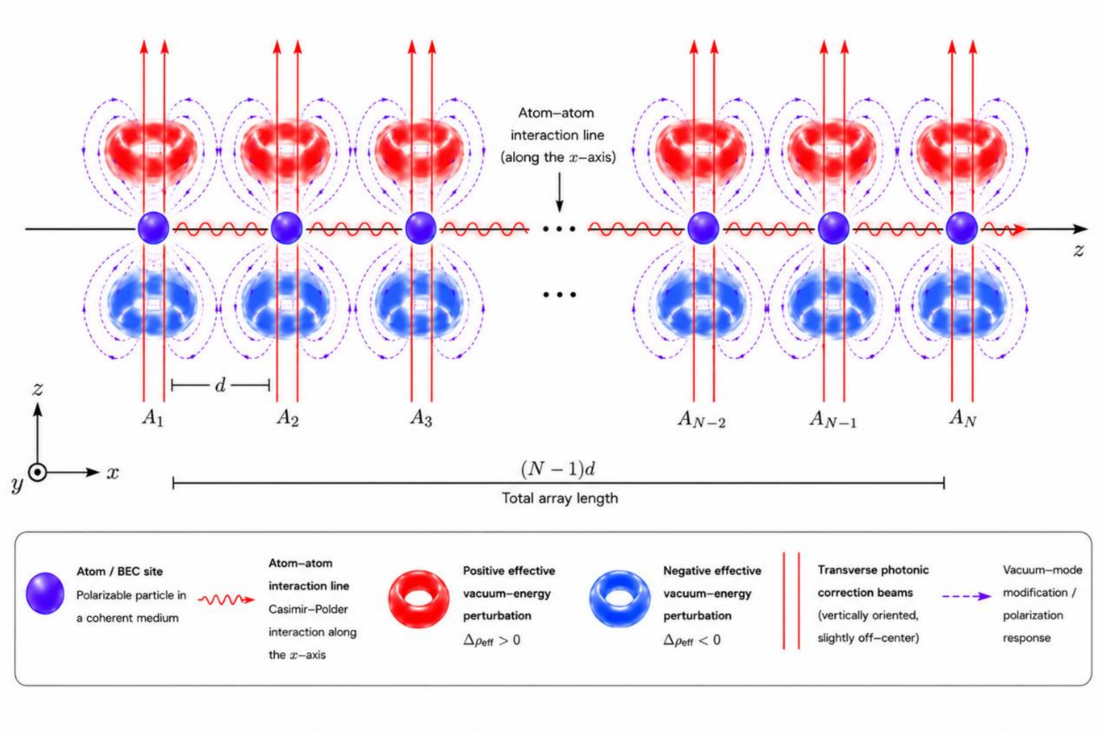

Figure 3. Conceptual schematic of a one-dimensional BEC atomic array aligned along the x-axis with transverse photonic correction along the z-axis.

In the proposed configuration, the compensation field is formed within the volume enclosed between two closely spaced concentric spherical shells. This volume is subdivided into sections containing ultracold neutral atoms prepared in the Bose-Einstein condensate (BEC) state.

It is necessary that the resulting structured field regions remain coherently aligned with respect to the effective gravitational-potential gradient generated by the propulsion core. In the proposed configuration, the lower effective potential region is oriented toward the inner core volume, corresponding to a common inward-directed vector, analogous to a radially inward effective-potential gradient.

The Casimir-Polder interaction can be interpreted as a manifestation of modified vacuum fluctuations in the presence of boundaries [10], [15, pp. 1185-1190], [16, pp. 1-10].

In this framework, variations in the effective vacuum energy density associated with structured Casimir geometries lead to corresponding changes in the local field correlations, which in turn determine the Casimir-Polder interaction strength.

While no universal proportionality coefficient exists, the interaction can be qualitatively related to the effective vacuum energy density through the atomic polarizability and the local spectral density of vacuum fluctuations.

The BEC chambers are located in the outer shell of the device in such a way that they occupy the entire surface of the housing at the same level and are connected to each other by adjacent walls made of magnetically permeable material. All Casimir cavities of each BEC chamber will be oriented identically relative to the radial symmetry of the apparatus body.

Each chamber hosts a spatially extended atomic ensemble realized in a quasi-uniform trapping potential, such as an optical box trap. Phase continuity between neighboring atomic ensembles in neighboring BEC chambers is maintained by coherent photon processing, resulting in a phase-synchronized atomic environment.

This combined regime has been demonstrated in experiments on uniform condensates and photon-mediated coupling of atomic ensembles, and does not require a single localized condensate occupying the entire volume [17].

The Casimir-Polder interaction and Casimir cavity fields do not represent separate fields, but different manifestations of a single quantum electromagnetic field. The apparent discreteness arises from boundary-induced mode quantization rather than from intrinsic discreteness of the field itself.

The compensation field is modeled as an effectively continuous medium formed by a dense array of Casimir-type cavities. While individual Casimir configurations are inherently discrete, it is well established that structured arrays at sufficiently small scales can be described within an effective-medium approximation [16], [18, pp. 400-414], [19, pp. 1780-1782].

In the present conceptual framework, the compensation field is assumed to arise from a phase-coherent network of Casimir-type cavities embedded within the BEC-layered structure. Each cavity produces a local vacuum-energy-density asymmetry associated with the corresponding Casimir-Polder interaction region.

When neighboring cavities remain phase-synchronized through the collectively coherent atomic medium and photonic coupling network, the resulting local vacuum-energy-density gradients are assumed to share a common orientation relative to the compensation-field geometry.

In the weak-field regime, sufficiently small local metric perturbations may be treated within the linearized approximation of general relativity, where individual perturbations superpose approximately linearly [1, Ch.18: weak gravitational fields; Ch. 35: linearized gravity and gravitational waves], [3, pp. 418-430: weak-field metric perturbations; pp. 430-440: linearized Einstein equations].

Under these assumptions, the local contributions are treated not as randomly oriented perturbations but as forming a partially coherent macroscopic stress distribution. The effective field strength therefore scales with the number of participating interaction regions, subject to the coherence and geometric reduction factors introduced later in the model.

In the conceptual picture adopted here, propulsion is interpreted as transport of the local effective field configuration rather than conventional acceleration through a fixed background space.

3. Pulse System: Dynamic Warp Bubble

This work introduces a conceptual model of a propulsion system grounded in a dynamically adjusted space-time configuration akin to a warp bubble. The system employs multiple energy sources ("warp cores") arranged along the direction of motion, whose energy densities are varied in time with a controlled phase shift.

The warp cores and the compensation field are modulated in a strictly phase-coherent manner, sharing a common temporal phase at each spatial location. A global phase lag is introduced as a function of position along the propulsion axis, giving rise to a traveling-wave-like modulation of the field configuration. This mechanism produces a sustained directional gradient of the effective spacetime deformation.

This approach enables stable propagation of the deformation pattern and prevents the formation of counter-propagating or reverse pulses. The proposed propulsion mechanism can be interpreted as a traveling-wave-driven transport of a localized spacetime deformation. While the concept of motion via a warp metric originates from the Alcubierre solution [6, pp. L73-L77], the present approach introduces a dynamic modulation of the field configuration.

The resulting behavior is analogous to transport mechanisms driven by propagating phase structures, where a traveling-wave modulation produces a net directional effect without requiring symmetric back-and-forth motion [20, pp. 284-295], [21, pp. 3-11], [22, pp. 799-825].

In this framework, the effective displacement of the system arises from the continuous forward shift of the deformation region, while the local frame of the payload remains approximately comoving.

The stability of the configuration critically depends on phase synchronization between the energy modulation of the cores and the compensation field. Symmetric energy distributions minimize vacuum-energy-induced stresses on the structure, while deviations from symmetry introduce loads that scale with the energy-density imbalance across the system.

The proposed approach suggests that controlled, low-amplitude oscillations of the field energy may be sufficient to induce directional motion, provided that the modulation amplitude and phase coherence are maintained within stability limits determined by the coherence properties of the compensation-field network.

The modulation amplitude is introduced as a small dimensionless parameter $\eta_{drive} = \Delta E/E_{tot}$. In the present work, a representative value $\eta_{drive} = 1\%$ is adopted, consistent with the weak-perturbation regime typically assumed in linearized treatments of spacetime deformation [2, pp. 70-75], [1, pp. 426-430].

The underlying energy density is modeled in terms of effective vacuum-energy variations associated with Casimir-type configurations [17, pp. 50-60], providing a physically motivated scale for the field energy distribution.

In the proposed configuration, the warp core is implemented as a spatially distributed structure extending along the length of the vehicle, enabling continuous modulation of the field energy rather than discrete localized sources.

To generate artificial gravity, it is required that an effective potential difference exists between the inner surface of the hull and the region occupied by the distributed core field. This potential difference must remain negligible compared to the primary modulation amplitudes associated with the propulsion system, in order to avoid additional structural loading and to preserve the stability of the field configuration.

A key design requirement is the orthogonality between the gradients associated with propulsion and artificial gravity. By maintaining these gradients perpendicular to each other, the artificial-gravity field does not interfere with the phase-coherent modulation responsible for directional propulsion, because orthogonal components of the field interact minimally [20, pp. 284-295], just as with small perturbations [1, pp. 942-948].

In this framework, the effective potential associated with the core region is maintained below that of the surrounding compensation field, such that the inner hull surface defines the upper boundary of the potential well. This allows artificial gravity to persist even in the absence of net propulsion (i.e., under static conditions).

Matching the local free-fall acceleration inside the bubble to Earth's gravity does not by itself guarantee identical time flow. In general relativity, clock rates depend on the gravitational potential rather than its gradient [2, pp. 165-170], [23, pp. 284-287]. Therefore, identical acceleration fields may correspond to different gravitational time dilation unless the potential is globally matched.

The system behavior under partial or complete deactivation of the compensation field during motion requires separate analysis, as it may lead to transient stress conditions and loss of controlled field structure.

Deceleration can be achieved by reversing the phase structure of the modulation, thereby generating an oppositely directed field gradient.

4. Gyroscope System & Navigation System

Navigation and control

The navigation system may be based on onboard sensors measuring distortions of background radiation fields, such as stellar or cosmological signals, induced by local spacetime deformation. These measurements provide a reference for trajectory control within the deformed metric.

Modern navigation systems already require relativistic temporal corrections predicted by general relativity [1, pp. 157–164; 297–302]. In particular, Global Positioning System (GPS) satellites compensate for both gravitational and kinematic time dilation effects [24]. Recent advances in optical atomic clocks and relativistic geodesy [25, pp. 662-666] additionally demonstrate that local gravitational potential differences may be measured through proper-time variations [24, 25].

Within the proposed framework, onboard sensor systems may therefore be extended beyond metric-gradient detection toward continuous mapping of local temporal gradients relative to a terrestrial reference frame.

Regions exhibiting minimal divergence of proper-time flow relative to Earth may hypothetically form effective isochronous navigation corridors for relativistic or warp-assisted travel. Transit through such regions could minimize temporal desynchronization between spacecraft crews and Earth-based observers during long-duration missions.

In this interpretation, navigation is determined not only by spatial trajectory optimization, but also by maintenance of a near-Earth synchronization state of the local spacetime geometry.

Directional control of the system can be achieved by coordinated modulation of the energy density of the surface (compensation) field and the distributed warp core. Controlled spatial displacement of the energy distribution generates a corresponding shift in the deformation pattern. This modulation must remain phase-coherent across all subsystems in order to maintain a stable and directed gradient of spacetime deformation.

The compensation-field structure may be interpreted as an inhomogeneously controlled array of Bose–Einstein condensate regions. It is well established that ultracold atomic systems can be structured into spatially resolved and independently addressable configurations, for example in optical lattices [26] and atom-chip–based traps [27].

Moreover, experimental techniques enable site-resolved control and manipulation of atomic populations, supporting the feasibility of spatially modulated and dynamically controlled condensate arrays [28, pp. 74–77], [29, pp. 68–72].

Operation without a warp core

In the absence of a warp core, the system reduces to a dynamically modulated compensation field. In this regime, directional effects may still arise from controlled asymmetries in the effective vacuum energy density (e.g., Casimir-type configurations). Such modulation can generate a directed gradient of the field distribution and, in principle, produce a net effective displacement.

However, without a central reference structure, the configuration becomes highly sensitive to perturbations. Small asymmetries or external influences may lead to instability of the deformation pattern, and the system loses a well-defined internal reference frame for controlled motion.

Role of system components

In the full configuration, the warp core and the compensation field play complementary roles. The warp core provides a stable reference structure for the local spacetime geometry, while the compensation field generates controlled differential deformations that enable propulsion.

In alternative operating modes, this interpretation may be inverted: the core may act as a primary driver of localized deformation, while the compensation field functions as a stabilizing and shaping mechanism.

This functional duality introduces a degree of redundancy into the system, allowing partial operation even under degraded conditions.

Potential extensions

The compensation field, considered independently, may also be interpreted as a platform for manipulating local field distributions. This suggests possible extensions to applications such as controlled modification of scattering signatures, precision navigation, or localized manipulation of effective field distributions, although such applications require further investigation.

5. Onboard AI

The proposed system involves the coordination of multiple high-complexity subsystems, each requiring real-time data processing and continuous exchange of information. The overall performance therefore depends critically on the reliability, synchronization, and integrity of distributed data flows across the system.

To address these requirements, a distributed data architecture may be employed, in which each subsystem operates as an autonomous node responsible for monitoring and controlling a specific functional component while maintaining a replicated data structure shared across the network. Such an approach enhances fault tolerance, as the failure of an individual node does not lead to loss of system-wide information or interruption of operation.

Efficient data exchange can be achieved by introducing hierarchical prioritization of information flows, allowing critical data to be transmitted with minimal latency while preventing overload of communication channels. This requires a structured protocol design that ensures stability under varying operational conditions.

Temporal synchronization between subsystems may be implemented using distributed clock-ordering and consensus mechanisms analogous to those used in fault-tolerant distributed computing systems [30], enabling consistent ordering of events and maintaining a coherent global time reference across distributed components.

Depending on the communication requirements, data structures may be organized into segmented blocks with defined interaction protocols. The inclusion of coordination mechanisms and predefined fallback procedures allows robust system behavior under degraded or emergency conditions.

The control requirements of the proposed system involve simultaneous processing of classical sensor data and potentially quantum-coherent subsystems. In this context, hybrid electronic–quantum processing architectures may provide a suitable platform for integrating high-throughput classical computation with quantum-state-aware control.

The need for such architectures arises from the combination of high-dimensional classical data streams and coherence-sensitive subsystems.

Architecture Based on Structured Casimir-Polder Interactions in BEC-Layered Cavities

i. Calculation of Magnetic and Photonic Fields

The BEC chamber hosts a spatially extended phase-coherent atomic medium realized via known BEC and optical trapping techniques.

Each chamber hosts a spatially extended atomic ensemble realized in a quasi-uniform trapping potential, such as an optical box trap. Phase continuity between adjacent atomic clouds is maintained via coherent photonic dressing, resulting in a collectively phase-locked atomic medium.

This combined regime has been demonstrated in experiments on uniform condensates and photon-mediated coupling of atomic ensembles, and does not require a single localized condensate occupying the entire volume [31].

The cooling mechanism required to reach the operational temperature range is not analyzed in detail in this work. It is assumed that established laser and evaporative cooling techniques [32, sec. 2], routinely used in Bose-Einstein condensation experiments, can be employed to prepare the atomic ensemble in the sub-microkelvin regime.

In the lunar shadow, the surrounding environment is characterized by a radiation temperature close to the cosmic microwave background (~3 K). The equilibrium temperature of a well-shielded structure is therefore determined primarily by radiative balance rather than by particle heating from the solar wind.

Although the trapping chambers are assumed to be integrated into the spacecraft structure, they are not considered to operate under microgravity conditions. Instead, a quasi-uniform artificial gravitational field, comparable to Earth's gravity, is assumed to be present at the deck level. Therefore, the trapping configuration is analyzed under standard gravitational conditions.

The confinement mechanism is functionally separated between the optical and magnetic components: the optical trap provides the dominant force for gravitational confinement, while the magnetic field defines and controls the spin-dependent properties of the atomic ensemble.

Magnetic Field

Parameters for calculating the magnetic field of BEC ensemble confinement in BEC chambers:

$L = 2\text{m}$;
$W = 1\text{m}$;
$h = 2 \times 10^{-3}$ m;
Particles: Cs-133;

$m_{Cs133} = 2.21 \times 10^{-25}$ kg;

$\mu_0 = 4\pi\times10^{-7}$ H/m;

$\mu_{eff} \approx \mu_B \approx 9.27\times10^{-24}$ J/T – order-of-magnitude estimate;

μ_{eff} – effective magnetic moment;

μ_B – Bohr magneton;

$k_B \approx 1.38\times10^{-23}$ J/K;

$T = 1$ μK [33], [34, pp. S83-S87];

The atom should not fly out of the chamber by the thickness of z:

$z_{max} = h/2 = 1\times10^{-3}$ m;

Thermal energy of an atom:

$E_{thermal} = k_B\times T$;

1. The condition for holding an ensemble of atoms in a BEC chamber:

$$U(z) \geq k_B\times T,$$

$$U(z) = m\omega_z^2 z^2/2,$$

$$m\omega_z^2 z_{max}^2/2 \geq k_B\times T,$$

$$\omega_z \geq \sqrt{2kB\times T/mz_{max}^2},$$

$$\omega_z \geq \sqrt{2\cdot1.38\times10^{-23}\cdot10^{-6}/2.21\times10^{-25}\cdot10^{-6}} \approx 11.17\ \mathrm{rad/sec}.$$

Trapping frequencies in magnetic BEC traps are typically in the range 10-10^3 Hz [35, pp. 40-55], [37, pp. 25-35].

2. Calculation of the magnetic field curvature:
Near the minimum of the field:

$$B(z) = B_0 + \beta z_{max}^2/2,$$

Magnetic potential for low-field seeking states:

$$U(z) = \mu_{eff}[B(z) - B_0] = \mu_{eff}\cdot\beta z_{max}^2/2,$$

Harmonic potential:

$$U_{harm}(z) = m\omega_z^2 z_{max}^2/2,$$

$$\mu_{eff} \cdot \beta = m\omega_z^2,$$

$$\beta = m\omega_z^2/\mu_{eff},$$

$$\beta = 2.21 \times 10^{-25}(11.17)^2/9.27 \times 10^{-24} \approx 2.97\ \mathrm{T/m^2}$$ [35, pp. 33-36].

3. Checking the depth of the magnetic trap:

At the edge of the area $z_{max} = 10^{-3}$ m:

$$\Delta B = \beta z_{max}^2/2,$$

$$\Delta B = 2.97 \times (10^{-3})^2/2 \approx 1.485 \times 10^{-6}\ \mathrm{T},$$

Trap depth:

$$U_{mag.trap} = \mu_B \Delta B,$$

$$U_{mag.trap} = 9.27 \times 10^{-24} \cdot 1.485 \times 10^{-6} \approx 1.38 \times 10^{-29}\ \mathrm{J} \approx k_B \times T.$$

4. A bias magnetic field in the range of a few Gauss is routinely used in Ioffe Pritchard type traps to prevent Majorana losses.

Take $B_0 = 10^{-4}$ T [34, pp. S87-S92], then:

$$B(z) = B_0 + \beta z^2/2,$$

$$B(z) \approx 10^{-4} + 1.49 z^2,$$

$$B(z_{max}) \approx 10^{-4} + 1.49 \cdot 10^{-6} = 1.0149 \times 10^{-4} \rightarrow B_0 >> \tfrac{1}{2}\beta z^2.$$

5. The field in the working volume of the BEC chamber is approximately uniform:

$$E_B \approx B^2 V/2\mu_0,$$

$$V = L \cdot W \cdot h,$$

$$E_B \approx (1.0149)^2 \times 10^{-8} \cdot 2 \cdot 2 \times 10^{-3}/8\pi \times 10^{-7} \approx 1.6 \times 10^{-8}\ \mathrm{J};$$

For engineering margin, take:

$$E_B = 3 \times 10^{-8}\ \mathrm{J};$$

Coils of the following parameters are usually used for such magnetic traps:

$I \sim 10 - 100$ A, $R \sim 0.1 - 1\ \Omega$ [33, pp. 235-245];

$1\ \mathrm{W} \le P_{mag} \le 10^4\ \mathrm{W}$.

Photonic Field

A quasi-electrostatic optical dipole trap based on a CO_2 laser at 10.6 µm was chosen for the optical confinement stage, following cesium trapping schemes in which photon scattering is negligible in this wavelength range.

The optical dipole potential is modeled following Grimm et al. (2000) [38], while the choice of a CO_2 laser at 10.6 µm is based on cesium experiments demonstrating negligible photon scattering (Weber et al.) [39].

Parameters for optic trap:

λ_L = 10.6 µm [39];

$P_{\text{lazer beam}}$ = 80 W [38, pp. 95-100], [39], was chosen in order to increase the peak intensity and, consequently, the trap depth;

w_0 = 100 µm [38, pp. 100-105] - beam waist, a beam waist was chosen in order to increase the peak intensity and, consequently, the trap depth, since peak intensity I ~ $1/w_0^2$.

1. The condition of particle retention in the gravitational field:

$$|dU_{\text{opt\_trap}}/dz| \geq mg,$$

$$U_{\text{opt\_trap}} \geq mg\Delta z,$$

$$U_{\text{opt\_trap}} \geq mgh,$$

$$U_{\text{opt\_trap}} \geq 2.21 \times 10^{-25} \cdot 9.8 \cdot 2 \times 10^{-3} \approx 4.33 \times 10^{-27}\ \text{J};$$

For engineering margin, take: $U_{\text{opt\_trap}} = 6 \times 10^{-27}$ J;

$U_{\text{opt\_trap}}/k_B = 6 \times 10^{-27}/1.38 \times 10^{-23} \approx 4.35 \times 10^{-4}$ K.

2. Rayleigh length:

$$z_R = \pi w_0^2/\lambda_L,$$

$$z_R \approx 3.14 \cdot 10^{-8}/10.6 \times 10^{-4} \approx 2.96 \times 10^{-4}\ \text{m};$$

3. Peak intensity:

$$I_0 = 2P_{\text{lazer\_beam}}/(\pi w_0^2),$$

$$I_0 \approx 2 \cdot 80/(3.14 \cdot 10^{-8}) \approx 50.93 \times 10^8\ \text{W/m}^2;$$

4. Radial frequency:

$$\omega_r = \sqrt{4U_{\text{opt.trap}}/mw_0^2}\ ,$$

$$\omega_r \approx \sqrt{4 \cdot 4.33^{\times}10^{-25}/2.21^{\times}10^{-25} \cdot 10^{-8}} \approx 2.80^{\times}10^{4}\ \text{rad/sec;}$$

5. Axial frequency:

$$\omega_z = \sqrt{2U_{\text{opt.trap}}/mz_R^2}\ ,$$

$$\omega_z \approx \sqrt{2 \cdot 4.33^{\times}10^{-25}/2.21^{\times}10^{-25} \cdot 2.96^{2\times}10^{-8}} \approx 0.67^{\times}10^{4}\ \text{rad/sec.}$$

As a reference, optical box traps are commonly implemented using a minimal configuration of one tube-like beam and two sheet-like beams, forming a closed trapping region [33], [40].

For the purpose of optical power estimation, the rectangular trapping region is modeled using a four-beam far red-detuned configuration. The beams are oriented transversely to the primary interaction axis, providing effective confinement and photonic field structuring in the plane perpendicular to the dominant Casimir-Polder interaction direction.

This four-beam representation is used as an effective engineering model for estimating optical power requirements and does not imply that the final implementation must be limited to four independent laser sources.

Laser installation power for the entire BEC chamber:

$$P_{\text{opt}} = 4 \cdot P_{\text{lazer\_beam}} = \mathbf{320\ W}.$$

ii. Calculation of Casimir-Polder Force for Pair of Atoms

The use of pairwise Casimir-Polder interactions as effective building blocks of the collective condensate response follows the common practice of deriving first-order scaling estimates from microscopic interactions. The quantitative values obtained here should therefore be regarded as phenomenological engineering estimates whose validation would require dedicated many-body numerical simulations and experimental calibration.

The frequency of the cesium atom Cs-133 line D1 ($6s_{1/2} \rightarrow 6p_{1/2}$; $\lambda \approx 894$ nm) and line D2 ($6s_{1/2} \rightarrow 6p_{3/2}$; $\lambda \approx 852$ nm), was used to estimate the boundary between the non–retarded and retarded modes of Casimir-Polder interaction as first shown by Casimir and Polder [10, p. 360].

The long-wave line D1 shifts the boundary of the retardation to large distances, shifting the crossover to larger distances:

$$\delta_{ret} \sim c/\omega_0$$ [41], [16, pp. 260-265],

where ω_0 – atomic transition frequency; for atom Cs-133:

Line D1: $\omega_0 = 2.1 \times 10^{15}$ rad/sec:

$$\delta_{ret1} \approx 3 \times 10^8 / 2.1 \times 10^{15} \approx 1.43 \times 10^{-7} \text{ m};$$

Line D2: $\omega_0 = 2.21 \times 10^{15}$ rad/sec:

$$\delta_{ret2} \approx 3 \times 10^8 / 2.21 \times 10^{15} \approx 1.36 \times 10^{-7} \text{ m};$$

Considering that the interaction takes place on two ranges with a retarding boundary δ_{ret}: $[\delta_{min}, \delta_{ret}] \cup [\delta_{ret}, \delta_{max}]$, $\delta_{min} = 6 \times 10^{-10}$; 5.3×10^{-10} m - the diameter of the cesium atom: below this limit, the Casimir force no longer acts, as strong repulsive forces arise, $\delta_{max} = 10$ μm.

The Casimir force formula for a pair of identical atoms:

$$F_{n\text{-}ret} = F_{cas}(\delta),\ \delta \in [6 \times 10^{-10}, \delta_{ret}],$$

$$F_{ret} = F_{cas}(\delta),\ \delta \in [\delta_{ret}, 10^{-5}];$$

$$F_{n\text{-}ret}(\delta) = -\,6/\delta^7 \cdot C_6,$$

$$C_6 = 3\hbar/\pi \cdot \int_0^\infty \alpha 2(i\xi) d\xi$$ [42, pp. 184-186],

$$\alpha^2(i\xi) = 2/3\hbar\ \Sigma_k\ (\omega_{k0}|d_{k0}|^2/(\omega^2_{k0}+\xi^2))$$ [43, pp. 245-252],

$$C_6 = 3\hbar/4 \cdot \alpha^2(0)\omega_0$$ [44, pp. 19–28],

where:

C_6 – van der Waals dispersion coefficient determined by the dynamic polarizabilities of the interacting atoms,

ξ[1/sec] – imaginary frequency variable,

$i\xi$ – imaginary frequency: $\omega_0 \rightarrow i\xi$;

$$|F_{n\text{-}ret}(\delta)| = (9\hbar/2\delta^7) \cdot \alpha^2(0)\omega_0$$ [10, pp. 360], [16, pp. 255-270],

$$|F_{ret}(\delta)| = (161\hbar \cdot c \cdot \alpha(0)^2)/(4\pi \cdot \delta^8)$$ [10, pp. 360], [16, pp. 255-270];

Where:

$\alpha(0) \approx 5.94 \times 10^{-29}$ m^3 is the polarizability coefficient of the cesium atom;

δ is the distance between atoms;

$\hbar \approx 1.05 \times 10^{-34}$ J·sec, - reduced Planck constant;

ω_0 – atomic transition frequency.

Substituting, we get approximately for D1 line:

$$E_{Cas} = E_{n\text{-}ret} + E_{ret},$$

$$E_{Cas} = \int_{\delta min}^{\delta ret} (9\hbar/2\delta^7) \cdot \alpha^2(0)\omega_0 \, d\delta + \int_{\delta ret}^{\delta max} (161\hbar \cdot c \cdot \alpha^2(0))/(4\pi \cdot \delta^8) d\delta,$$

$$E_{Cas} = 27(\hbar \cdot \alpha^2(0)\omega_0)(1/\delta_{min}{}^6 - 1/\delta_{ret}{}^6) +$$

$$+ 5.75[(\hbar \cdot c \cdot \alpha(0)^2)/\pi](1/\delta_{ret}{}^7 - 1/\delta_{max}{}^7),$$

$$E_{n\text{-}ret} = 27(1.05 \times 10^{-34} \cdot 35.28 \times 10^{-58} \cdot 2.1 \times 10^{15}) \times$$

$$\times (1/(6^6 \times 10^{-60}) - 1/(1.43^6 \times 10^{-42})) \approx 0.45 \times 10^{-18} \text{ J};$$

$$E_{ret} = 5.75[(1.05 \times 10^{-34} \cdot 3 \times 10^8 \cdot 35.28 \times 10^{-58})/\pi] \times$$

$$\times (1/(1.43^7 \times 10^{-49}) - 1/10^{-35}) \approx 1.66 \times 10^{-34} \text{ J};$$

$$E_{Cas} \approx 0.45 \times 10^{-18} \text{ J};$$

$$F_{Cas} \approx E_{n\text{-}ret}/(\delta_{ret} - \delta_{min}) = 0.45 \times 10^{-18} /(1.43 \times 10^{-7} - 6 \times 10^{-10}) \approx$$

$$\approx 0.32 \times 10^{-11} \text{ N};$$

Line D2:

$$E_{Cas} = \int_{\delta min}^{\delta ret} (9\hbar/2\delta^7) \cdot \alpha^2(0)\omega_0 \, d\delta + \int_{\delta ret}^{\delta max} (161\hbar \cdot c \cdot \alpha^2(0))/(4\pi \cdot \delta^8) d\delta,$$

$$E_{Cas} = 27(\hbar \cdot \alpha^2(0)\omega_0)(1/\delta_{min}{}^6 - 1/\delta_{ret}{}^6) +$$

$$+ 5.75[(\hbar \cdot c \cdot \alpha(0)^2)/\pi](1/\delta_{ret}{}^7 - 1/\delta_{max}{}^7),$$

$$E_{n\text{-}ret} = 27(1.05 \times 10^{-34} \cdot 35.28 \times 10^{-58} \cdot 2.1 \times 10^{15}) \times$$

$$\times (1/(6^6 \times 10^{-60}) - 1/(1.36^6 \times 10^{-42})) \approx 0.45 \times 10^{-18} \text{ J};$$

$$E_{ret} = 5.75[(1.05 \times 10^{-34} \cdot 3 \times 10^8 \cdot 35.28 \times 10^{-58})/\pi] \times$$

$$\times (1/(1.36^7 \times 10^{-49}) - 1/10^{-35}) \approx 2.36 \times 10^{-34} \text{ J};$$

$$E_{Cas} \approx 0.45 \times 10^{-18} \text{ J};$$

$$F_{Cas} \approx E_{n\text{-}ret}/(\delta_{ret} - \delta_{min}) = 0.45 \times 10^{-18} /(1.43 \times 10^{-7} - 6 \times 10^{-10}) \approx$$

$$\approx 0.32 \times 10^{-11} \text{ N};$$

Both lines:

$$E_{Cas} \approx 0.45{\times}10^{-18} + 0.45{\times}10^{-18} = 0.9{\times}10^{-18}\ J;$$

$$F_{Cas} \approx 0.32{\times}10^{-11} + 0.32{\times}10^{-11} = 0.64{\times}10^{-11}\ N;$$

The obtained value should be interpreted as an order-of-magnitude estimate based on the adopted interaction model and integration limits.

It is necessary to set the Casimir-Polder interaction field for the entire volume of BEC chambers. The paper proposes to consider two ways:

1. the configuration of the interaction field of neutral atoms in a BEC ensemble;

2. the configuration of the interaction field of the BEC ensemble with monatomic polarized surface deposition arranged vertically in a row parallel to the side of the chambers equal to 1 meter, at distances of no more than 10 μm between them.

Both methods of interaction can be applied in the design of BEC chambers. This will eliminate the need to create a huge number of partitions inside the BEC chambers and eliminate the need to create time-consuming atomic spraying, which will significantly reduce the cost of the technology.

iii. Interactions of a BEC Atomic Ensemble with a Monatomic Polarized Surface Lattice

Since the Casimir-Polder interaction is carried out between the atoms of the BEC ensemble with atoms sprayed on a flat surface and arranged in a discrete lattice, a formula reflecting the atom-atom interaction with the summation of interactions at the nodes is chosen to calculate the Casimir-Polder force.

Assume that the shape and size of the ship's hull is an ellipsoid with a surface area equal to that of a sphere with a radius of $r = 100$ m, the surface of which is covered with a layer of BEC thickness $\varepsilon = 2$ mm. Shell volume:

$$V \approx 4\pi r^2 \cdot \varepsilon = 4\pi \cdot (100)^2 \cdot 2{\times}10^{-3} \approx 248.36\ m^3,$$

Assume that chamber size is 2 meters ×1 meter ×2mm. The thickness of the bulkheads between the chambers is 2 mm, thickness of the plates inside the chambers - 5 μm, distance between plates - 20 μm, the plates will be positioned parallel to the short side of the chamber. Then:

Chamber volume: $0.004 - 4{\times}10^{-6} \approx 0.004\ m^3$;

Volume of plate: $10^{-8}\ m^3$;

Number of chambers: $\approx 248.36/0.004 \approx 62{,}090$;

Number of plates: $62{,}090\cdot(2 - 2{\times}10^{-3})/(5{\times}10^{-6} + 2{\times}10^{-5}) \approx 4.96{\times}10^{9}$;

Volume of plates: $10^{-8}\cdot 4.96{\times}10^{9} = 49.6$ m^3;

Volume of bulkheads: $12{\times}10^{-6}\cdot 62{,}090 = 0.74$ m^3;

BEC ensemble total volume: $248.36 - 49.6 - 0.74 = 198.02$ m^3;

If the density of interacting atoms in BEC $\rho_{BEC} = 10^{21}$ atoms/m^3 (maximum) that total number of moving atoms is:

$$N_{BEC} = 10^{21}\cdot 198.02 \approx 1.98{\times}10^{23};$$

The minimum center-to-center separation was chosen as $r_{min} = 6{\times}10^{-10}$-$7{\times}10^{-10}$ m, corresponding to approximately twice the van der Waals radius of Cs. This choice avoids significant overlap of the electronic shells and provides a conservative lower bound for the atom–atom separation.

At smaller separations, electronic wavefunction overlap and short-range repulsive interactions become non-negligible.

In a dense hexagonal package, the atoms number of surface deposition per square meter:

$$\rho_{spr.} = 2/(\sqrt{3}\cdot r_{min}^2),$$

$$S_{spr} = 2\cdot(4.96{\times}10^{9} + 62{,}090)\cdot 2{\times}10^{-3} \approx 1.98{\times}10^{7}\ \text{m}^2,$$

$$N_{spr.} = S_{spr}\cdot 2/(\sqrt{3}\cdot r_{min}^2),$$

$$N_{spr.} = 1.98{\times}10^{7}\cdot 2/(\sqrt{3}\cdot 49{\times}10^{-20}) \approx 0.47{\times}10^{26};$$

Since the interaction occurs with a symmetrical geometry, uniform density, and under a laser correction field, approximate formulas can be obtained to estimate the number of interacting atoms for approximate calculations that approximately take into account the dynamics of particle motion and the solid angle of interaction.

The typical solid angle value for a laser-corrected BEC is from π to 2π steradians [38, pp. 95–170].

Let's take an angle of π for conservative calculations: $\Omega = \pi$ sr, then:

$$\eta_\Omega = \Omega/4\pi,$$

$$\eta_\Omega = 0.25.$$

Due to the small contribution of the energy of the retarded interaction mode, we will take into account only the non-retarded:

1. Not all atoms interact, but only pairs at a distance less than $1.36{\times}10^{-7}$ m.: $\delta_{ret\_eff} = \min\{\delta_{ret1}, \delta_{ret2}\}$. This means that each BEC atom interacts with the number of surface deposition atoms that fit in a

circle formed by the intersection of the sputtering plane and a cone with guide = $1.36{}^{\times}10^{-7}$ m and a vertex in the center of the BEC atom.

The radius of the circle depends on the distance of the BEC atom from the deposition surface and will vary from zero to the ~ 0.7 radius of interaction ($S \sim 0.49\pi\ R^2$):

$$\langle r^2 \rangle = (0.7R^2)/2,$$

$$\langle r^2 \rangle = 0.245\ R^2,$$

$$S_{eff} = \pi \langle r^2 \rangle,$$

$$S_{eff} \approx 0.245\pi R^2.$$

Such geometric reduction factors are consistent with constrained atom–surface interaction models [10].
As an approximation, let's take the average value $S \sim 0.25\pi\ R^2$.

At a distance $7{}^{\times}10^{-10}$, the atoms stop interacting, which means that the radius of the cone's circle with this height is maximal, but the difference between the cone's base (height = $7{}^{\times}10^{-10}$, guide = = $1.36{}^{\times}10^{-7}$) and the circle of the cone with zero height is negligible. Total number of interacting atoms K:

$$S \approx 0.25\pi\cdot \delta_{ret}{}^2,$$

$$S \approx 0.25\cdot 3.14\cdot 1.85{}^{\times}10^{-14} \approx 1.45{}^{\times}10^{-14}\ m^2,$$

$$K_{spr.} = S\cdot \rho_{spr.},$$

$$K_{spr.} \approx 1.45{}^{\times}10^{-14}\cdot 2/(\sqrt{3}\cdot 49{}^{\times}10^{-20}) \approx 3.42{}^{\times}10^4;$$

2. On the other hand, the number of BEC atoms with which each sprayed atom interacts is placed in the volume of the figure formed by the intersection of a sphere with a retardation radius, a sphere with a radius $\delta = 6{}^{\times}10^{-10}$, and a cone with a vertex in the center of the sprayed atom and an angle $\Omega = \pi$ sr. For a simplified formula, we assume that a sphere with a smaller radius is a point.

$$K_{BEC} \sim \rho_{BEC}\cdot \pi\delta_{ret}{}^3/3,$$

$$K_{BEC} \approx 3.14\cdot (1.36)^3{}^{\times}10^{-21}\cdot 10^{21}/3 \approx 2.63;$$

3. Total number of interaction pairs:

$$N_{pairs} = (N_{BEC}\cdot K_{spr.} + N_{spr.}\cdot K_{BEC})/2,$$

$$N_{pairs} = (1.98{}^{\times}10^{23}\cdot 3.42{}^{\times}10^4 + 0.47{}^{\times}10^{26}\cdot 2.63)/2 \approx$$

$$\approx 0.677{\times}10^{28} + 1.236{\times}10^{26} \approx 0.69{\times}10^{28};$$

4. A conservative geometric reduction factor $\eta_{geo} = 0.6$ is introduced to account phenomenologically for nonideal packing, shielding, and incomplete directional coherence, consistent with effective-medium treatments and reduced-accessibility corrections commonly used in structured many-body systems [19, pp. 1780–1782], [37, pp. 235–289]:

$$N_{total} \approx \eta_{\Omega} \cdot \eta_{geo} \cdot N_{pairs} \approx 0.25 \cdot 0.6 \cdot 0.69{\times}10^{28} \approx 0.1{\times}10^{28};$$

The present estimates neglect explicit contributions from photon scattering, technical noise, finite-temperature fluctuations, and residual decoherence. For the selected trapping parameters, far-detuned optical confinement regime, and assumed phase-stabilized operation, these effects are expected to contribute primarily as higher-order corrections not included explicitly in the present estimate. Their influence is therefore absorbed phenomenologically into the reduction coefficients η_{geo} and η_{Ω}, and is not treated separately in the present order-of-magnitude analysis.

Total Casimir force:

$$\mathbf{F_{total}} = F_{Cas} \cdot N_{total} \approx 0.64{\times}10^{-11} \cdot 10^{27} \approx \mathbf{0.64{\times}10^{16}\ N};$$

$$\mathbf{E_{total}} = E_{Cas} \cdot N_{total} \approx 0.9{\times}10^{-18} \cdot 10^{27} \approx \mathbf{0.9{\times}10^{9}\ J};$$

iv. Interactions Between Atoms of BEC Atomic Ensemble

Assume that chamber size is 2 meters ×1 meter. The thickness of the bulkheads between the chambers is 1 mm. Then:

Shell volume: $\approx 248.36\ m^3$;

Chamber volume: $\approx 0.004\ m^3$;

Number of chambers: ≈ 62,090;

Volume of bulkheads: $12{\times}10^{-6} \cdot 62{,}090 = 0.74\ m^3$;

BEC ensemble total volume: $248.36 - 0.74 = 247.62\ m^3$;

$\rho_{BEC} = 10^{21}$ atoms/m^3;

$\eta_{\Omega} = 0.25$;

Representative phenomenological coefficients:

The factor $\eta_{coh} = 0.9$ accounts for a modest reduction of ideal coherent participation caused by weak interatomic perturbations, residual many-body back-action, and small phase fluctuations within the condensate. A 10% reduction is adopted as a conservative allowance for such effects. [35]

The factor $\eta_{shield} = 0.85$ accounts for shielding-related reduction of effective interactions. In dense ensembles, not all nominal interaction pairs remain equally accessible because neighboring atoms may partially screen or suppress interaction pathways. [37]

The factor $\eta_{crowd} = 0.8$ accounts for local many-body crowding effects, i.e. the reduction of ideal pair accessibility caused by neighboring atoms perturbing or partially obstructing one another at short range. This factor represents a local steric and many-body correction and is distinct from the solid-angle factor η_Ω which accounts only for directional limitations of the interaction geometry [19, pp. 1780–1782]. Then:

$$\eta_{BEC} = \eta_{coh} \cdot \eta_{shield} \cdot \eta_{crowd},$$

$$\eta_{BEC} = 0.9 \cdot 0.85 \cdot 0.8 = 0.612 \approx 0.6;$$

$$N_{BEC} \approx 10^{21} \cdot 247.62 \approx 2.48 \times 10^{23},$$

$$N_1 = N_2 = 0.5 N_{BEC},$$

$$K_1 = K_2 = K_{BEC},$$

$$K_{BEC} \sim \rho_{BEC} \cdot \pi \delta_{ret2}^3 / 3,$$

$$K_{BEC} \approx 2.63,$$

$$N_{total} = \eta_\Omega \cdot \eta_{BEC} \cdot K \cdot N_{BEC}/2,$$

$$N_{total} = 0.25 \cdot 0.6 \cdot 2.63 \cdot 2.48 \times 10^{23}/2 \approx 0.49 \times 10^{24};$$

$$\mathbf{F_{total}} = F_{Cas} \cdot N_{total} \approx 0.64 \times 10^{-11} \cdot 0.49 \times 10^{24} \approx \mathbf{0.31 \times 10^{13}\ N};$$

$$\mathbf{E_{total}} = E_{Cas} \cdot N_{total} \approx 0.9 \times 10^{-18} \cdot 0.49 \times 10^{24} \approx \mathbf{0.44 \times 10^{6}\ J};$$

v. Quantitative Estimation of Casimir-Polder Interaction Network

Photonic field

The photonic correction fields of adjacent BEC chambers are assumed to be partially coupled through coherent tunneling and boundary-mediated optical overlap within the compensation medium. In the present model, this coupling is treated phenomenologically through an effective pairwise optical coupling coefficient.

The pairwise coupling between two adjacent chambers i and j is approximated as:

$$k_{ij}^{opt} = \mathrm{R}_{\mathrm{eff}}\cdot(\mathrm{A}_{\mathrm{overlap}}/\mathrm{A}_{\mathrm{ch}})\cdot\cos\theta_{\mathrm{ij}}\cdot N_{ref}^{eff}\cdot(1+\cos\varphi_{\mathrm{ij}})/2,$$

Where:
N_{ref}^{eff} - the number of possible internal reflections (2-5);
$\mathrm{R}_{\mathrm{eff}} = 0.9$ [46, pp. 2-3] - the proportion of reflected/retained light;
$\mathrm{A}_{\mathrm{overlap}}/\mathrm{A}_{\mathrm{ch}}$ - geometric factor of connection between BEC chambers;
$\cos\varphi_{\mathrm{ij}}$ - taking into account the orientation between the optical axes of the BEC chambers;
$\theta_{\mathrm{ij}} \sim 0°\text{-}15°$ - angle of incidence of the wave [47, pp. 282-284]; for different sections of an ellipsoid elongated along the same axis, the angle values will vary from zero and above;
$(1+\cos\varphi) \sim 1$ is the phase factor [48, pp. 289-293]:

$$\varphi_{\mathrm{ij}} = 4\pi n d_{\mathrm{ij}}\cdot\cos\theta_{\mathrm{ij}}/\lambda_{\mathrm{L}},$$

where:
$n = 1.00012\text{-}1.00025$ - effective refractive index [49, p. 2];
$d_{\mathrm{ij}} = 2$ mm is the characteristic separation between reflecting boundaries;
$\lambda_{\mathrm{L}} = 10.6$ μm - wavelength of the control field (Cs-133: D1 transition $6\mathrm{S}_{1/2} \to 6\mathrm{P}_{1/2}$; $\lambda \approx 894$ nm, and D2 transition $6s_{1/2} \to 6p_{3/2}$; $\lambda \approx 852$ nm) [50, pp. 47-50].

$$\mathrm{A}_{\mathrm{overlap}} = 4\times10^{-3}\ \mathrm{m}^2,$$

$$\mathrm{A}_{\mathrm{ch}} = 2\ \mathrm{m}^2,$$

$$k_{ij}^{opt} \approx 0.9\cdot(4\times10^{-3}/2)\cdot0.97\cdot1\cdot3\cdot1/2 = 2.62\times10^{-3};$$

Because the BEC correction chambers are distributed over an ellipsoidal hull, the coupling coefficient is not spatially uniform. Both the local chamber power and phase must therefore be adjusted individually in order to compensate for geometric variations and maintain coherent alignment across the compensation array.

At the array level, the resulting correction field is described as a coherent superposition of chamber contributions:

$$\mathrm{U}_{\mathrm{total\_opt}} = \Sigma_{j=1}^{N}\mathrm{U}_{\mathrm{j}}\, e^{\varphi_{\mathrm{ij}}},$$

$$\mathrm{U}_{\mathrm{total\_opt}} \approx k_{ij}^{opt}\mathrm{N}_{\mathrm{chambers}}\cdot\mathrm{U}_{\mathrm{opt.trap}},$$

$$\mathrm{U}_{\mathrm{total\_opt}} \approx 2.62\times10^{-3}\cdot62{,}090\cdot6\times10^{-25} \approx 976\times10^{-25} \approx 9.76\times10^{-23};$$

$$\mathrm{K}_{\mathrm{E}} = \mathrm{U}_{\mathrm{total\_opt}}/\mathrm{U}_{\mathrm{opt.trap}} \approx k_{ij}^{opt}\mathrm{N}_{\mathrm{chambers}},$$

$$K_E \approx 1.63 \times 10^2;$$

$$K_I = I_{total}/I_0 \approx (k_{ij}^{opt} N_{chambers})^2,$$

$$K_I \approx 2.65 \times 10^4.$$

This representation makes it possible to distinguish clearly between amplitude reinforcement and intensity amplification. In the fully phase-aligned limit, the field amplitudes add constructively, whereas the corresponding intensity scales quadratically with the resulting amplitude.

In this framework, the optical coherence coefficient does not modify the intrinsic physical scale of the Casimir-Polder interaction itself; rather, it provides a coherence-weighted normalization of the correction-field amplitude distributed across the compensation network. The quantitative values of the effective coupling coefficients must ultimately be calibrated experimentally, since the degree of coherent reinforcement depends on the detailed cavity geometry, reflection properties, and phase stability of the laboratory implementation.

Optical deflectors (e.g., AOD [51, pp. 52-60], SLM [52, pp. 169–175], or MEMS or integrated photonic switching architectures [53, pp. 4, 3–5] -based beam steering systems) may be employed to dynamically control the spatial distribution, phase, and amplitude of photonic correction fields. This allows multiplexing of laser sources and coherent addressing of extended atomic ensembles, while reducing the number of required emitters.

Compensation field

A collective coherence parameter γ may be introduced as a qualitative higher-order correction describing possible many-body enhancement in the interaction array. In a conservative estimate, one may assume:

$$1 < \gamma < \sqrt{N_{pairs}};$$

by analogy with collective coherent scaling. However, in the present work this parameter is not included explicitly as a multiplicative factor in the total force, in order to avoid double counting with the optical coherence coupling already incorporated into the compensation-field model.

A possible overlap between collective many-body coherence effects and the photonic coherence coupling already included in the compensation-field model cannot be excluded. For this reason, the parameter γ is not applied as an additional multiplicative factor in the force estimate, in order to avoid double counting.

Following White et al. (2021) [8], structured Casimir cavities may produce nontrivial vacuum-energy density distributions whose geometry has been argued to exhibit qualitative similarities to warp-metric energy profiles. In the present model this correspondence is represented by an effective coupling coefficient η_{cavity}, describing the fraction of Casimir vacuum-energy density asymmetry contributing to the macroscopic compensation-field configuration.

The Casimir compensation field does not represent an energy reservoir that is depleted during operation, but a boundary-condition-induced vacuum-energy configuration. Its stability time is therefore limited primarily by mechanical, thermal, electromagnetic, and phase-coherence stability of the cavity architecture, rather than by decay of the Casimir effect itself.

Calculation of Power and Energy of the Entire Engineering System

i. Optical Power and Energy of the Fiber-Core System

In the present work, the warp core is modeled as a photonic energy anchor whose primary function is not strict field coherence, but localized storage and controlled delivery of electromagnetic energy. The total optical power is determined by:

$$P_{opt} = 2nP_{stream},$$

while the energy simultaneously present in the core is estimated as:

$$E_{core} = P_{opt}\, L \cdot n_g / c.$$

The operating condition of the subsystem is defined by the energy-matching relation:

$$E_{core} \sim E_{field},$$

which sets the scale of the required optical power and pulse parameters. The phase-interleaved pulsed structure is used primarily to smooth power delivery and reduce thermal loading, rather than as a strict coherence requirement.

$$P_{opt} = E_{field} \cdot v_g / L,$$

Where:
P_{opt} – optical power of the warp core;
v_g – photon pulse velocity in the waveguide;
L – waveguide length.

The speed of pulse propagation in the fiber:

$$v_g \sim c / n_g,$$

Where:
$n_g \approx 1.45\text{-}1.5$ – A representative group index is adopted for silica-based waveguides [45, Ch. 22];

c – velocity of light;

$$N_{cont} = 2n,$$

$$P_{stream} = P_{opt}/2n,$$

$$P_{stream} \sim E_{field} \cdot c/(2n \cdot n_g \cdot L),$$

Where:
P_{stream} – the power of one continuous stream;
n – number of waveguides of one phase;
N_{cont} – number of continuous streams.

Each laser channel operates in a duty-cycle-limited pulsed regime. A pulse of duration τ is followed by an idle interval of 2τ, giving a repetition period T = 3τ and a duty factor D = 1/3. Therefore, the average power of one channel is:

$$P_{pulse} = 1/3 \cdot P_{stream};$$

Duty factor:

$$D = 3\nu\tau \lesssim 1/3 \Rightarrow P_{pulse} \sim P_{stream}/3,$$

Where:
P_{pulse} – optical power of one pulse;
ν – a pulse repetition frequency;
τ – pulse duration.

$$P_{pulse} \approx 0.9{\times}10^{9} \cdot 3{\times}10^{8}/6n \cdot 1.5 \cdot L,$$

$$P_{pulse} \approx 0.3{\times}10^{17}/n \cdot L \text{ [W]};$$

We take 1 MW for the power value of one laser, which is technically feasible [54]. Then:

$$0.3{\times}10^{17}/n \cdot L = 10^{6},$$

$$n \cdot L = 3{\times}10^{10} \text{ [m]},$$

An effective waveguide length of 10 km is adopted as an engineering compromise between increased photon residence time and practical limitations associated with optical losses, nonlinear effects, dispersion, and thermal management. [55]. Then lifetime of a photon pulse in a warp anchor waveguide:

$$t_{res} = L \cdot n_g/c,$$

$$\mathbf{t_{res} \approx 50\ \mu s;}$$

$$\boldsymbol{n = 3 \times 10^6;}$$

$$E_{pulse} = P_{pulse} \cdot \tau,$$

$$\nu = 1/9\tau,$$

$$\mathbf{\nu \approx 0.11 \times 10^5\ Hz;}$$

$$\mathbf{\tau \approx 33\ \mu s,}$$

$$\mathbf{T \approx 100\ \mu s;}$$

$$\mathbf{E_{pulse}} \approx 10^6 \cdot 33 \times 10^{-6} = \mathbf{33\ J;}$$

$$P_{opt} = E_{field} \cdot v_g / L,$$

$$v_g \sim c/n_g,$$

$$v_g \approx 3 \times 10^8 / 1.5 = 2 \times 10^8\ \mathrm{m/sec},$$

$$\mathbf{P_{opt}} \approx 0.9 \times 10^9 \cdot 2 \times 10^8 / 10^4 = \mathbf{1.8 \times 10^{13}},$$

$$\eta_{laser} = P_{opt}/P_{el},$$

where:
P_{el} – a conservative effective efficiency is adopted at the system level, including optical conversion losses and baseline thermal-management overhead;
η_{laser} = 30% - A conservative wall-plug efficiency [7, pp. 567–577],

$$\mathbf{P_{el}} = 1.8 \times 10^{13}/0.3 = \mathbf{6 \times 10^{13}\ W}.$$

For simplicity, the adopted efficiency parameter is treated as an effective engineering efficiency that includes both conversion losses and first-order cooling overhead.

The resulting total power demand is estimated to be of order 6×10^{13} W i.e. in the tens-of-terawatts range. This should be interpreted as an upper-bound order-of-magnitude requirement for the present configuration rather than a near-term engineering power target.

ii. Photonic Core Energy Scale and Localization Metrics

Because the absolute value of vacuum energy in quantum field theory is not directly accessible in laboratory Casimir measurements, the macroscopic energy-scale estimate is referenced to the observed cosmological vacuum-energy density. This quantity is used only as a background normalization scale, whereas the Casimir contribution is treated as a local differential vacuum-energy effect associated with boundary conditions.

Therefore, the cosmological vacuum-energy density is not assumed to be identical to the Casimir energy density. Instead, it provides a conservative large-scale reference value for estimating the volume over which an equivalent amount of background vacuum energy would be distributed.

The parameter $K_\lambda = R_\lambda^3/r_{sh}^3$ is introduced as a volume concentration ratio, comparing the macroscopic volume containing an equivalent amount of cosmological vacuum energy with the local working volume of the system. This factor should not be interpreted as a direct energy-reduction coefficient, but rather as a scaling indicator for how strongly the field energy must be localized in the proposed configuration.

Vacuum energy density:

$$u_\lambda = c^4\lambda/8\pi G;$$

$$u_\lambda \approx 5\times10^{-10}\ \mathrm{J/m^3}\ [56];$$

Equivalent volume:

$$V_\lambda = E_{core}/u_\lambda,$$

$$R_\lambda = (3E_{core}/4\pi u_\lambda)^{1/3};$$

The local operating volume is approximated by the characteristic enclosed volume of the ship, on the assumption that the effective spatial influence of the gravitational anchor is confined by the surrounding compensation field:

$$V_{work} = 4/3\ (\pi r_{sh}^3),$$

$$K_\lambda = (3E_{core}/4\pi u_\lambda)/r_{sh}^3,$$

$$K_\lambda = (3\cdot0.9\times10^9/4\pi\cdot5\times10^{-10}\cdot10^6) = 0.43\times10^{13}.$$

Linear localization ratio, providing a characteristic measure of the spatial concentration scale of the core energy:

$$K_{linear} = (3E_{core}/4\pi u_\lambda)^{1/3}/r_{sh},$$

$$K_{linear} = (3\cdot0.9\times10^9/4\pi\cdot5\times10^{-10})^{1/3}/10^2 = 0.75\times10^4.$$

The localization ratios K_λ and K_{linear} are introduced only to characterize the spatial concentration of the energy scale. They are not applied as multiplicative or divisive factors in the calculation of the required optical core energy.

iii. Entire Engineering System Power

The total power required for one BEC chamber is estimated as:

$$P_{ch} = P_{mag} + P_{opt} \approx 10500\ \mathrm{W} \approx 11\ \mathrm{kW},$$

for entire field system:

$$P_{field} = 62{,}090 \cdot 11 \approx 68.2\ \mathrm{MW};$$

Now we calculate the length for the shape of the cigar model in the approximation of a cylinder plus two hemispheres.
Let's take the radius of the cylinder r equal to 40 m - a convenient value for a multi-deck ship, radius of hemispheres l = 5 m, L - cylinder length:

$$S = 2\pi rL + 4\pi r^2 = 4\pi R^2,$$

$$1.26{\times}10^5 = 80\pi L + 6{,}400\pi,$$

$$80\pi L \approx 1.26{\times}10^5 - 20{,}106,$$

$$250L \approx 106{,}000,$$

$$L \approx 424\ \mathrm{m},$$

$$d = L + 2l,$$

$$d = 434\ \mathrm{m};$$

We will calculate the volume of the warp anchor based on the fact that its thickness is 2 m, and the length and width will be approximately equal to the length (d) and width (2r) of the entire apparatus:

$$V = 69{,}440\ \mathrm{m}^3;$$

The volumetric heat generation may reach $q \sim 10^7\text{-}10^9\ \mathrm{W/m^3}$, which is comparable to the ranges observed in nuclear reactor cores and high-power accelerator targets. Power of the warp core cooling unit:

$$P_{cool} = q \cdot V,$$

$$P_{cool} \approx 6.9{\times}10^{13}\ \mathrm{W}.$$

The power of the entire warp core installation:

$$P_{core} = P_{cool} + P_{el},$$

$$P_{core} \approx 6.9{\times}10^{13} + 6{\times}10^{13} \approx 1.3{\times}10^{14}\ W;$$

total engine power:

$$P_{total} = P_{core} + P_{field},$$

$$\mathbf{P_{total} \approx 1.3{\times}10^{14}\ W.}$$

iv. Field-Stress Estimates and Structural Load Transfer

The Casimir force is assumed to act along the effective gravitational-potential gradient [1, pp. 426-445]. The corresponding average field-stress proxy on the hull surface is estimated as:

$$\sigma_{field} = F_{total}/4\pi R^2,$$

$$\sigma_{field} = 0.64{\times}10^{16}/1.26{\times}10^{5} \approx 5.1{\times}10^{10}\ Pa;$$

When the amplitude of the warp core energy fluctuations is 1%, the internal distributed field-stress proxy acting on the ship's hull is estimated at the bulkhead surfaces as:

$$\sigma_\tau = 0.01\cdot F_{total}/(N_{chambers}\cdot S_{bulkhead});$$

$$\sigma_\tau = 0.01\cdot 0.64{\times}10^{16}/(62{,}090\cdot 2\cdot 0.2) \approx 2.58{\times}10^{9}\ Pa;$$

The resulting value should not be interpreted as a classical mechanical stress acting directly on the hull material. It is introduced only as an effective field-stress scale associated with the distributed deformation field.

The mechanical fraction transferred to the hull is represented by a phenomenological coupling coefficient η_{load}, analogous to energy-transfer and participation factors commonly employed in structural dynamics and vibration analysis [57, Ch. 2-3]:

$$0 < \eta_{load} << 1.$$

The actual mechanical stress acting on structural materials is assumed to be:

$$\sigma_{mech} = \eta_{load}\cdot\sigma_{field},$$

$$\sigma_{mech\_\tau} = \eta_{load}\cdot\sigma_\tau.$$

It is likely that the transverse bulkheads in the BEC chambers may require reinforcement by vertical struts. One of the main materials for the calculation can be a polymer reinforced with carbon fiber (CFRP, $\rho_{material} \approx 1500$ kg/m^3), used in the aerospace industry. This material has high strength, flexibility and elasticity at the same time.

The quantity F_{total} should be interpreted as an effective collective interaction scale characterizing the distributed Casimir-Polder network. It does not represent a directly measurable external force acting on the spacecraft and is introduced only as a proxy for estimating the magnitude of the associated field-stress distribution.

Effective Dynamics and Scaling Estimates

The dynamics of the system is estimated by introducing an effective gravitational-potential difference associated with the total available system energy. Following the weak-field interpretation in which energy acts as the source of gravitation [2, Ch. 3], the characteristic potential scale is assumed to be proportional to the total system energy:

$$E_{field} = E_{core} = 0.9{\times}10^9 \text{ J},$$

$$|\Delta\Psi_0| \sim E_{total}/M_{eff} = E_{field}/M_{eff} + E_{core}/M_{eff}.$$

Since the systems of the gravitational armature and the compensation field oscillate synchronously:

$$\Delta\Psi_0(t) = \Delta\Psi_{core}(t) + \Delta\Psi_{field}(t),$$

$$|\Delta\Psi_0| = \chi_{\psi,\,core} \cdot E_{core} / M_{eff} + \chi_{\psi,\,field} \cdot E_{field} / M_{eff},$$

where:

M_{eff} - an effective mass introduced to characterize the dynamical response of the system to the imposed potential gradients. This quantity does not represent the physical rest mass of the structure, but rather an equivalent parameter relating the applied force to the resulting acceleration;

$0 < \chi_\psi < 1$ is a dimensionless coupling coefficient bounded between zero and unity.

By definition, χ_ψ represents the fraction of the total system energy contributing to the effective gravitational potential and is therefore constrained to values between zero and unity.

The parameter χ_ψ is introduced as an effective dimensionless coupling coefficient characterizing the fraction of the total system energy that contributes to the effective gravitational potential [58, pp. 1-26]. Since the underlying microscopic coupling mechanism is not specified within the present framework, χ_ψ is treated as a phenomenological parameter whose value must ultimately be determined experimentally. To obtain an optimistic upper-bound estimate, the limiting case $\chi_\psi = 1$ is adopted.

The acceleration is estimated from the spatial gradient of the effective potential generated by the full system energy. Let's take the amplitude of fluctuations in the energy of warp cores equal to η_{drive} = 1% of their energy. Then the acceleration formula [1, Ch. 18, pp. 432-445]:

$$a_{eff} = \nabla\Psi_{osc} \approx \Delta\Psi_{osc}/d,$$

$$\Delta\Psi_{osc} = \eta_{drive} \cdot \Delta\Psi_0,$$

where d - the length of the aircraft along the direction of travel.

Assume that the gravitational potential oscillates like a sine wave anticipating the energy fluctuations of the system in the aft part relative to the bow itself $\Delta t = 0.1T$:

$$\phi = 2\pi\Delta t/T,$$

$$\phi \approx 0.628 \text{ rad},$$

$$\Delta\Psi(t) = \Delta\Psi_0 \cdot (1 + \eta_{drive} \cdot \sin(2\pi t/T - \phi \cdot x/d)),$$

the period of synchronous pulsation of warp core energy and compensation fields.

$$a_{eff} = \eta_{drive} \cdot \Delta\Psi_0 \cdot 0.628/d.$$

To calculate the length of the body *d*, we will take the surface area of a sphere with a radius of 100 m, since the system is computationally linked to this area through the number of BEC chambers. Let's calculate the length for the shape of the cigar model in the approximation of a cylinder plus two hemispheres.

For an elongated hull of length 434 m and radius 40 m, the total volume is of order $2{\times}10^6$ m^3. Assuming an effective structural density $\rho_{eff} \approx 100 - 300$ kg/m^3, the corresponding mass is estimated as $M_{ship} \approx 10^7 – 10^8$ kg.

$$a_{eff} \approx 0.01 \cdot 1.8{\times}10^9 \cdot 0.628/(10^7 \cdot 434) \approx 2.6{\times}10^{-3} \text{ m/sec}^2,$$

take η_{drive} = 10%; for the stability of the system, we take 10 layers of the compensation field:

$$a_{eff} \approx 0.1 \cdot 1.8{\times}10^{10} \cdot 0.628/(10^7 \cdot 434) \approx 2.6{\times}10^{-1} \text{ m/sec}^2,$$

For this characteristic acceleration the classical timescale to reach relativistic velocities is of order ~ 40 years.

Let's calculate how large the difference between the gravitational potential of the core and the potential of the compensation field at the inner surface of the envelope will be required for a favorable acceleration of free fall, for example g_g = 9.8 m/sec^2:

$$|g_g| = |\nabla_g\Psi_0| = \Delta_g\Psi_0/h = |\Psi_{field} – \Psi_{core}|/h,$$

$$\nabla_g\Psi_0 \perp \nabla\Psi_0 => \Delta\Psi_0 \perp \Delta_g\Psi_0 => g_g \perp a_{eff},$$

where h – the distance from the center to the surface of the warp core, in this case, is 1 meter.

$$\Delta_g\Psi_0 = 9.8\ \mathrm{m}^2/\mathrm{sec}^2,$$

$$\Delta_g\Psi_0 = \eta_g \cdot \Delta\Psi_0,$$

$$\eta_g = \Delta_g\Psi_0/\Delta\Psi_0,$$

$$\eta_g = 9.8\cdot 10^7/1.8\times 10^{10} = 5.44\times 10^{-3},$$

this value shows that the establishment of a gravitational field will not interfere with the operation of the system due to a slight deviation of the field energy from the core energy of about half a percent.

The temporal evolution of acceleration is governed by the modulation period:

$$j = 2\pi\cdot a_{eff}/T\ [\mathrm{m}/\mathrm{sec}^3],$$

$$\Delta t = 0.1T.$$

Modern PIC chips (Photonic Integrated Circuit) make it possible to control multiple lasers and fields, modulate the phases and delays of signals on multiple channels at the nanosecond level.

In contrast to conventional propulsion systems, the proposed concept does not rely on momentum exchange with expelled mass. Instead, the propulsion effect is described in terms of an effective force arising from the imposed potential gradients:

$$F_{eff} = -\ M_{eff} \cdot \nabla\Psi_{osc} \approx -\ M_{eff} \cdot \Delta\Psi_{osc}/d,$$

$$\mathbf{|F_{eff}|} \approx 1.8\times 10^{10}/434 = \mathbf{4.15\times 10^{7}\ N.}$$

For one-layer compensation field:

$$\mathbf{|F_{eff}| \approx 4.15\times 10^{6}\ N.}$$

Fiber-Optic Monitoring System for the Dynamic State of the Core

To monitor the dynamic state of the warp core and the associated elements of the gravitational armature, it is proposed to use a distributed fiber-optic sensor system based on recording changes in the optical signal during bending, microdeformation and vibration of the fiber. The basic engineering scheme of such a system is a spiral configuration of a single-mode fiber around a multimode channel, which makes it possible to determine the coordinate of a local disturbance based on the time difference between the arrival of signals and the change in their modulation. In the context of a warp core, such a system is considered not as a direct meter of field energy or space curvature, but as a highly sensitive structural feedback channel that records the mechanical and phase response of the bearing elements to a change in the operating mode of the core.

Sensor Configuration

Mechanical vibrations of an optical fiber integrated into a structural element lead to variations in the optical path length and to perturbations of the internal reflection conditions of the guided radiation (see Figure 4).

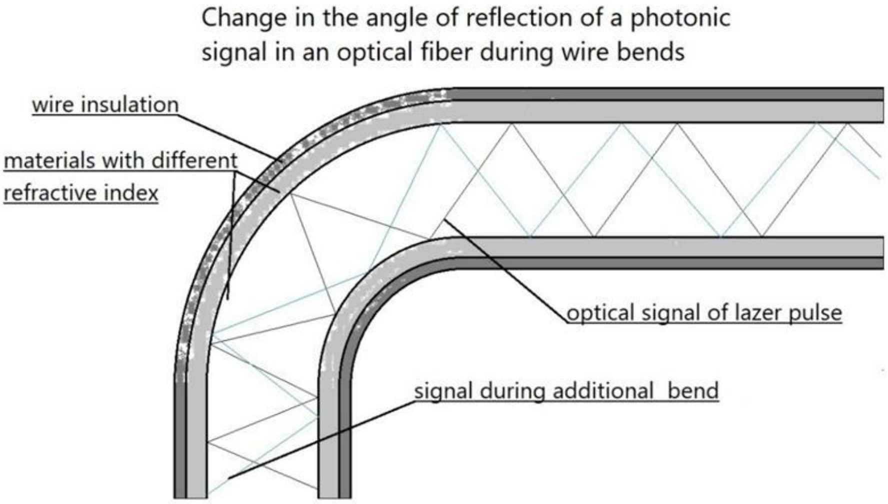

Figure 4. Optical losses induced by local bending of the fiber

The sensing cable consists of two optical fibers arranged within a common braid: a multimode fiber (MMF) and a single-mode fiber (SMF). The single-mode fiber is helically wound around the multimode fiber, forming a composite structure with different effective optical path lengths for signal propagation (see Figure 5).

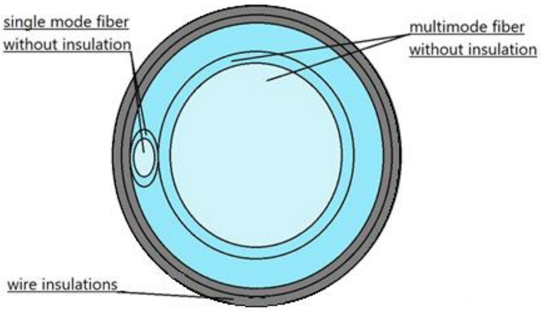

Figure 5.

The radiation source is coupled to one end of the multimode fiber, while the opposite end is connected to receiver 1. The single-mode spiral fiber is connected, at the source side, to a photodetector via a partially reflective optical element. At the opposite end, it is connected to receiver 2, as shown in Figure 6. The receivers and the photodetector convert the optical signals into electrical signals for further processing.

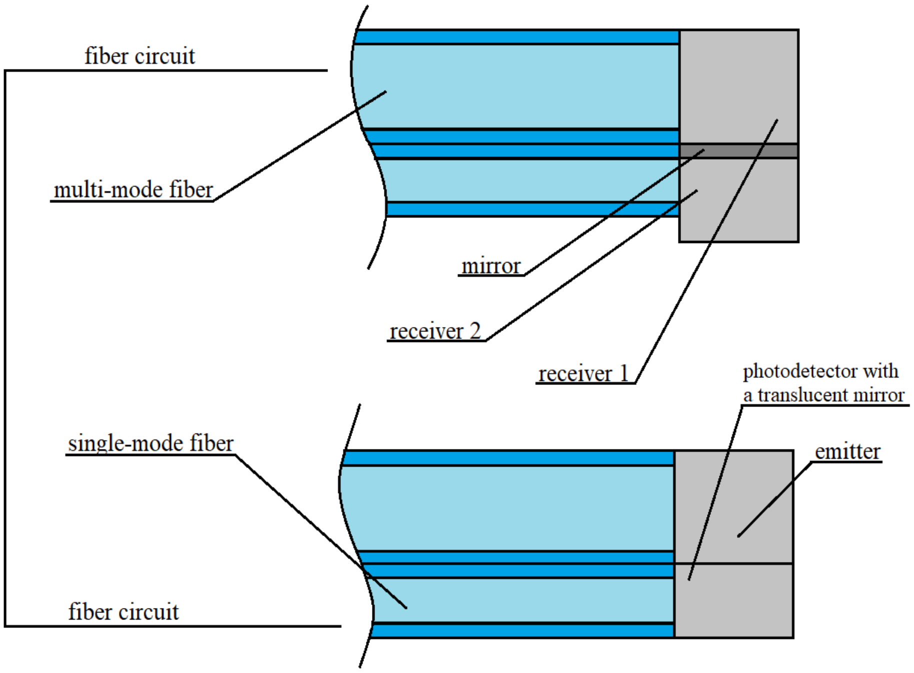

Figure 6. Optical sensing system layout

The receiver unit in the single-mode channel includes a photodetector and an optical element (e.g., a mirror or a metamaterial membrane) configured to reflect incident radiation at non-normal incidence angles, enabling controlled signal routing and detection - see Figure 7:

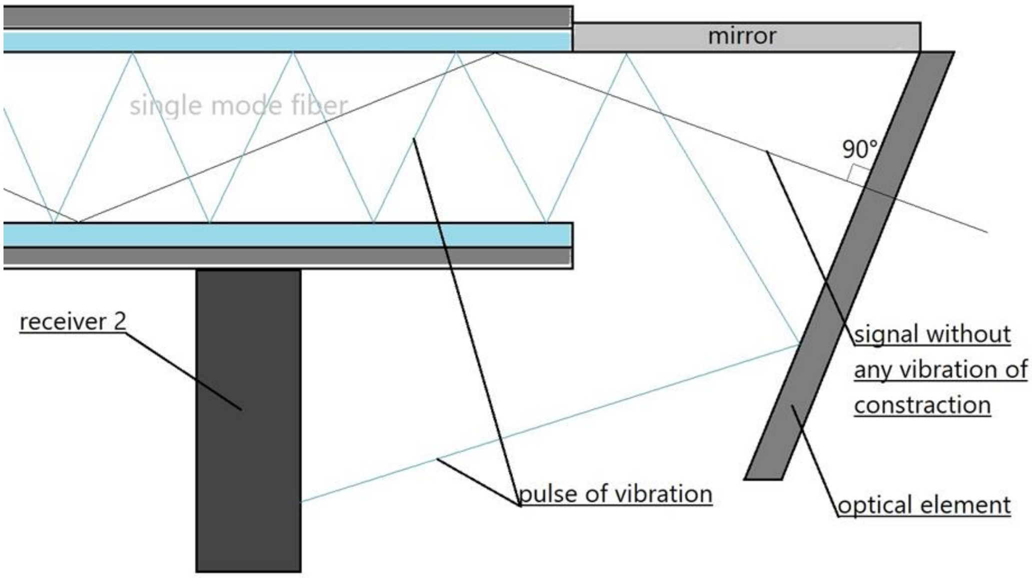

Figure 7. Single-mode receiver unit

This configuration enables differential signal timing and phase analysis for localization of perturbations along the sensing line.

During the initial calibration stage, the optical system is adjusted such that the radiation exiting the single-mode channel is incident normally on the optical element and is fully absorbed. Under these conditions, receiver 1 registers no signal, while receiver 2 records a stationary baseline response corresponding to the steady-state optical losses and intrinsic geometric configuration of the fiber.

In the nominal operating regime, structural vibrations induce a reproducible modulation of the optical signals in both channels due to strain-induced variations in optical path length and scattering losses. The corresponding temporal characteristics are recorded and stored as a reference state.

Deviations from the reference signals $S_1(t)$ and $S_2(t)$, representing the temporal responses of receiver 1 (MMF channel) and receiver 2 (SMF channel), respectively, are interpreted as indicators of anomalous structural perturbations. Due to the difference in effective optical path lengths, signals originating from the same perturbation arrive at the receivers with a time delay Δt, which is used for spatial localization.

The coordinate of the perturbation is reconstructed from the measured delay Δt using the analytical expressions derived in Section Calculation for the relationship between time delay and spatial position.

In the presence of multiple simultaneous perturbations, the received signals may form ambiguous pairs. To resolve this ambiguity, both forward and reverse propagation paths in the spiral channel are utilized, yielding a system of two independent equations for each candidate signal pair. Only those pairs for which the system admits a consistent (physically admissible) solution are considered valid.

The scattered radiation generated at a local deformation point propagates in both directions along the single-mode fiber. Although the exact distribution depends on geometric and modal parameters, it is assumed to be approximately symmetric on average for the purpose of statistical signal reconstruction.

The signal processing procedure is implemented as an adaptive algorithm (see Figure 8) that performs dynamic pairing of detected events and evaluates candidate solutions based on consistency criteria.

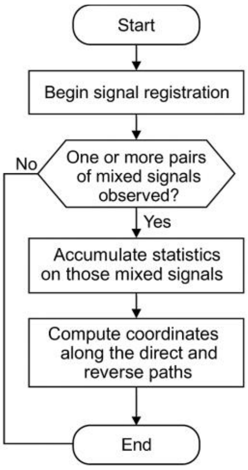

Figure 8.

The implementation of the described sensing and processing principles imposes specific constraints on the physical design of the cable. In practice, the system is realized for predefined cable lengths, each associated with a specific set of calibration constants, including the effective propagation velocity of light in the fiber, the spiral pitch, and the refractive indices of the optical media.

Since the minimum bending radius of a single-mode fiber is significantly larger than that of a multimode fiber, the cable design incorporates a compliant core that preserves flexibility while maintaining geometric stability. The radius of the core is selected to be comparable to the minimum bending radius of the single-mode fiber. For example, fibers of the G.657 standard exhibit minimum bend radii ranging from approximately 5 mm to 10 mm depending on the subclass.

Multimode fibers are arranged around the core in a single-layer configuration, forming the primary sensing channel. A single-mode fiber is then helically wound around this structure, providing a secondary channel with an increased effective optical path length. The insulation layer provides both optical isolation and mechanical protection while maintaining sufficient flexibility to preserve sensitivity to structural vibrations. The mechanical integrity of the core and insulation is critical, as variations in the spiral pitch may introduce systematic errors in the localization of perturbations.

The described configuration ensures the mechanical compliance and optical sensitivity required for reliable detection and localization of structural perturbations in complex engineering systems.

Analytical Model

Based on the minimum bending radius of a single-mode fiber, we assume for preliminary calculation the radius of the core with an environment of multimode fiber equal to 5 millimeters. Since the outer diameter of a standard optical fiber is 125 micrometers, the diameter of the core itself will be 9.750 millimeters.

Since the single-mode fiber is wound on a core with a multimode without gaps, the spiral pitch will be a multiple of the outer diameter of the fiber, i.e. 125 micrometers. Let's take the number of single-mode fibers equal to 48. Then the spiral pitch is 48*0.125 = 6.0 millimeters.

Spiral pitch (along the multimode fiber axis): 6 mm;
Multimode fiber diameter (without insulation): 125 μm;

The formula for the length of a cylindrical spiral in one step:

$$\mathrm{l} = \sqrt{(2\pi \mathrm{r})^2 + h^2},$$

where:
h = 6.0 mm – pitch of spiral;
r = 5.0 mm - radius;

$$l = \sqrt{(2\pi \cdot 0.005)^2 + (0.006)^2} \approx 0{,}032 \text{ m};$$

This means that for every 6 mm along the axis (multi-mode fiber), there is ≈ 32 mm of single-mode fiber.

$$x/x' = h/l,$$

$$x/x' = 3/16 = 0.1875,$$

where x/x' - the ratio of the lengths of a multi-mode fiber to a single-mode fiber in a cable section from the coordinate of the detected vibration to one of the cable ends.

Now we calculate the signal travel time over a 20-meter-long cable. The speed of light in a fiber:

$$V = c/n,$$

where:
n - refractive indices of the fiber core;
c – speed of light in absolute vacuum.
Time of passage over multimode optical fiber, taking into account pulse dispersion:

$$t = (L\cdot n_m)/c + \Delta t_{modal},$$

$$\Delta t_{modal} \approx (L\cdot n_m)/c \cdot \Delta/2,$$

where:
n_m - refractive index of multi-mode fiber: ≈ 1.48 - typical for quartz fiber;
Δ - the relative difference in the refractive indices of the fiber core and cladding, let's take the value for standard multimode fibers ≈ 0.01;
L = 20 m. - sensing system length.
The formula for relative difference in the refractive indices:

$$\Delta = (n^2_{core} - n^2_{clad})/2n^2_{core};$$

$$t_1 = (20\cdot 1.48)/3\cdot 10^8 + (20\cdot 1.48\cdot 0.01)/2\cdot 3\cdot 10^8 \approx 9.916\cdot 10^{-8} \text{ s} = 99.16 \text{ ns};$$

Time of passage over spiral single-mode optical fiber:

$$t = (L\cdot l\cdot n_s)/(c\cdot h),$$

where n_s - refractive index of single-mode fiber: ≈ 1.468 (typical for quartz fiber at 1.550):

$$t_2 = (20\cdot 0.032\cdot 1.468)/(0.006\cdot 3\cdot 10^8) \approx 52.196\cdot 10^{-8} \text{ s} = 521.96 \text{ ns};$$

Time difference (delay):

$$\Delta t \approx 422.80 \text{ ns}.$$

Now we will derive the equation for finding the coordinate from the time difference between the movement of the signal along different paths, taking into account the main corrections:

$$t_1 = x \cdot n_m/c + x \cdot n_m \cdot \Delta/2c,$$

$$t_2 = 16x \cdot n_s/3c,$$

$$\Delta t = 16x \cdot n_s/3c - (x \cdot n_m/c + x \cdot n_m \cdot \Delta/2c),$$

$$\Delta t = (32x \cdot n_s - 6x \cdot n_m - 3x \cdot n_m \cdot \Delta)/6c,$$

$$\Delta x_1 = (\Delta t \cdot 6c)/(32n_s - 6n_m - 3n_m \cdot \Delta);$$

The same equation is corrected for the case when the signal propagates in the opposite direction along the spiral fiber:

$$t_2 = (2L - x)/V_s,$$

$$t_1 = x \cdot n_m/c + x \cdot n_m \cdot \Delta/2c;$$

$$t_2 = 16(2L - x) \cdot n_s/3c,$$

$$\Delta t = 32L \cdot n_s/3c - 16x \cdot n_s/3c - (x \cdot n_m/c + x \cdot n_m \cdot \Delta/2c),$$

$$\Delta x_2 = (32L \cdot n_s/3c - \Delta t) \cdot 6c/(6n_m + 3n_m \cdot \Delta + 32n_s);$$

In the case of mixed pairs of signals from different vibration points, the controller solves both equations in one system for all possible combinations of pairs:

$$\Delta x_1 = (\Delta t \cdot 6c)/(32n_s - 6n_m - 3n_m \cdot \Delta),$$

$$\Delta x_2 = (32L \cdot n_s/3c - \Delta t) \cdot 6c/(6n_m + 3n_m \cdot \Delta + 32n_s).$$

Only those pairs out of all possible pairs for which this system is solvable are a pair of signals from one vibration point. In this case, having a solution to a system of equations means that both equations individually have the same solutions for the same pair of signals.

Now, let's calculate the accuracy of the localization of the vibration point based on the difference in the signal travel time. Assuming a timing resolution in the picosecond range ($\delta t \sim 10^{-12}$ sec), which is achievable in modern photonic detection systems using high-speed photodetectors and time-to-digital conversion electronics, the theoretical localization accuracy can be estimated as:

$$\Delta x_1 = (\Delta t \cdot 6c)/(32n_s - 6n_m - 3n_m \cdot \Delta),$$

$$\delta(\Delta x_1)/\delta t = 6c/(32n_s - 6n_m - 3n_m \cdot \Delta),$$

$$\delta x_1 = (10^{-12} \cdot 6 \cdot 3 \cdot 10^8)/(32 \cdot 1.468 - 6 \cdot 1.48 - 3 \cdot 1.48 \cdot 0.01) \approx \mathbf{0.047 \times 10^{-3}\ m};$$

Calculation of accuracy according to the signal of a single-mode fiber going in the opposite direction:

$$\Delta x_2 = (32L \cdot n_s/3c - \Delta t) \cdot 6c/(6n_m + 3n_m \cdot \Delta + 32n_s),$$

$$\delta(\Delta x_2)/\delta t = - 6c/(6n_m + 3n_m \cdot \Delta + 32n_s),$$

$$|\delta(\Delta x_2)| = 6c \cdot \delta t/(6n_m + 3n_m \cdot \Delta + 32n_s),$$

$$|\delta(\Delta x_2)| = 6 \cdot 3 \cdot 10^8 \cdot 10^{-12}/(6 \cdot 1.48 + 3 \cdot 1.48 \cdot 0.01 + 32 \cdot 1.468) \approx \mathbf{0.032 \times 10^{-3}\ m};$$

Since the two accuracy lines differ, we take the maximum value from them: **0.047×10^{-3} m.**

To calculate the entangled pairs of signals, you can use two such systems connected to a common controller in parallel, but without calculating the time for the signal reflected from the mirror. Both cables must be tightly clamped in a common braid of optical fibers of the same standard.

Let h_1 and h_2 denote the spiral pitches of the first and second sensing lines, respectively. To avoid degeneracy of the coordinate solutions, it is required that $h_1 \neq h_2$. The resulting difference in propagation-delay functions provides an independent localization criterion for identifying signal pairs originating from the same vibration point.

Then, in the case of several vibration locations, the controller program finds a solution to two equations of the same type for two pairs of signals, sorting through all possible pairs of signals. The pair of signals for which the solutions of the two equations coincide is a pair of signals from the same location of extraneous vibrations. Since pairs of signals are duplicated at different time intervals between the signals in the pair, the correspondence is uniquely identified.

The controller calculates only those signals that go in the forward direction, the photodetector in the opposite direction sends messages to the controller about the reverse signals and they are not processed.

let's calculate the parameters of the second cable by taking the spiral pitch h' value of 60 millimeters:

$$l' = \sqrt{(2\pi r)^2 + h'^2},$$

$$l' = \sqrt{(2\pi \cdot 0.005)^2 + (0.06)^2} \approx 0.068\ m;$$

This means that for every 60 mm along the axis (multi-mode fiber), there is ≈ 68 mm of single-mode fiber:

$$h'/l' \approx 0.882;$$

Time intervals and equation for coordinate:

$$t_1 = t'_1 = x_2 \cdot n_m/c + x_2 \cdot n_m \cdot \Delta/2c,$$

$$t_2 = 16x_2 \cdot n_s/3c,$$

$$t'_2 = 34x_2 \cdot n_s/3c,$$

$$\Delta t' = 17\Delta x_2 \cdot n_s/15c - (\Delta x_2 \cdot n_m/c + \Delta x_2 \cdot n_m \cdot \Delta/2c),$$

$$\Delta t' = \Delta x_2 \cdot (34n_s - 30n_m - 15n_m \cdot \Delta)/30c,$$

$$\Delta x_2 = (\Delta t' \cdot 30c)/(34n_s - 30n_m - 15n_m \cdot \Delta);$$

Calculation of accuracy for second line:

$$\delta x_2 = (10^{-12} \cdot 30 \cdot 3 \cdot 10^{8})/(34 \cdot 1.468 - 30 \cdot 1.48 - 15 \cdot 1.48 \cdot 0.01) \approx \mathbf{1.74{\times}10^{-3}\ m};$$

For the case of mixed pairs of signals from different vibration points:

$$\Delta x_1 = (\Delta t \cdot 6c)/(32n_s - 6n_m - 3n_m \cdot \Delta),$$

$$\Delta x_2 = (\Delta t' \cdot 30c)/(34n_s - 6n_m - 3n_m \cdot \Delta).$$

In practical fiber-based sensing systems, the effective accuracy may be limited by detector jitter, modal dispersion, thermal drift, optical losses, and signal-to-noise ratio. Therefore, to take into account the accuracy of the sensor, we take the value $\Delta t \sim 10^{-11}$ sec. Since the two accuracy lines differ, we take the maximum value from them: **$1.74{\times}10^{-2}$ m**.

The localization sensitivity depends on the ratio between the spiral and axial propagation lengths. Increasing the optical path difference between the multimode and single-mode channels improves timing sensitivity, whereas excessively large spiral pitches reduce the differential delay and therefore decrease localization accuracy.

A trade-off exists between localization sensitivity and signal-pair discrimination. The first sensing line should therefore employ a minimal spiral pitch to maximize timing sensitivity, whereas the second line should use a different, larger pitch chosen such that the resulting localization error remains within acceptable limits while still providing an independent localization criterion.

The intensity of the optical pulse coupled into the single-mode fiber is expected to depend on the local bending amplitude of the composite cable structure and, in particular, on deformation of the multimode fiber. Under fixed installation and calibration conditions, the corresponding transfer relation can be experimentally determined during the initial system setup.

Consequently, the amplitude of anomalous vibrations may be estimated from the intensity of the optical signal detected in the single-mode channel by the photodetector and receiver subsystem.

The bending radius of the spiral single-mode fiber is defined by the cable geometry and can be treated as a fixed system parameter. In contrast, the bending radius of the multimode fiber varies with the instantaneous deformation of the entire cable during vibration. Therefore, the signal amplitude detected in the single-mode channel is primarily governed by bending-induced scattering in the multimode fiber, while the spiral single-mode winding provides a calibrated distributed capture efficiency. Under this approximation, the detected amplitude may be written as:

$$P_{SMF}(t) \propto P_{MMF}(R_C(t)) \cdot \eta_{SMF}(R_{SMF,0}),$$

where:
$P_{SMF}(t)$ is detected optical intensity;
$R_C(t)$ is the instantaneous bending radius of the composite cable;
$R_{SMF,0}$ is the fixed bending radius of the spiral single-mode fiber;
$P_{MMF}(R_C(t))$ is the bending-induced scattered optical power generated in the multimode fiber;
$\eta_{SMF}(R_{SM,0})$ is the effective distributed capture efficiency of the spiral single-mode channel.

Parallel distributed sensor lines may provide an additional correlation criterion based on relative pulse intensity maxima, improving identification of mixed or partially overlapping signal pairs during simultaneous perturbation events.

If extended toward interferometric operation, the proposed sensing architecture could potentially provide sensitivity to extremely small variations in effective optical path length through differential phase measurements. In this respect, the concept bears a distant analogy to large-scale interferometric systems such as LIGO, where differential optical-path variations are used to detect strain-like perturbations [45, Ch. 19]:

$$\Delta\phi = (2\pi/\lambda) \cdot \Delta L,$$

where ΔL - effective optical path variation.

Such an approach could, in principle, be investigated as a possible method for probing extremely weak effective metric-like perturbations or distributed optical-path distortions in structured field environments.

In such a configuration, intensity-based measurements could provide localization and deformation amplitude estimates, while interferometric phase analysis could extend the sensitivity of the system toward extremely small distributed optical-path perturbations.

In principle, distributed sensor lines connecting the outer structure to the propulsion warp core could also be investigated as probes of effective acceleration-gradient-induced structural perturbations and differential optical-path variations within the artificial gravity environment.

Conclusions and Future Directions

This work presents an engineering-oriented theoretical framework for a propulsion concept based on structured Casimir-Polder interactions and collective quantum effects in confined systems. Unlike purely theoretical approaches to metric engineering, the proposed model emphasizes system architecture, controllability, and the integration of sensing and feedback mechanisms.

The spatial arrangement of subsystems follows from the requirement to localize the field-generating region while minimizing its influence on the operational volume. The propulsion core is positioned in the lower part of the structure, where energy conversion and thermal management systems are co-located to reduce transmission losses and simplify heat dissipation. The upper region is mechanically and functionally separated from the core, providing a stable operational environment for standard operations.

The lateral regions surrounding the core may exhibit reduced effective acceleration due to the imposed potential gradients, forming transition zones between dynamically distinct parts of the system. The resulting configuration supports the separation of operational and technical volumes, while enabling controlled gradients of effective potential within the structure.

Localized variations of the effective potential may give rise to regions with reduced apparent weight, which could facilitate handling and transport of massive objects within the system. Such effects, however, are constrained by the achievable field configuration and energy distribution.

A distributed fiber-optic sensing system is introduced as a means of monitoring the dynamic state of the field-generating structure. The proposed approach enables detection and spatial localization of perturbations through differential signal propagation, providing a basis for real-time diagnostics and control. The use of multiple sensing channels and adaptive signal processing allows the resolution of complex scenarios involving simultaneous perturbations.

This sensing capability is essential for maintaining stability of the proposed field configuration.

The analytical model establishes the relationship between signal delay and spatial coordinates, allowing estimation of localization accuracy under realistic assumptions about timing resolution and optical properties of the system. The results indicate that the achievable precision is primarily limited by timing resolution, dispersion effects, and stability of the optical and mechanical subsystems.

Although the proposed framework remains highly speculative and does not constitute a direct method for space–time metric manipulation, it provides a structured approach to exploring indirect mechanisms of force redistribution and field compensation.

A preliminary estimate of the required power levels for 10-layers compensation field:

$$E_{field} = E_{core} = 0.9 \times 10^{10} \text{ J},$$

$$P_{total} \approx 1.3 \times 10^{15}\ \text{W},$$

$$F_{eff} \approx 4.15 \times 10^{7}\ \text{N},$$

$$a_{eff} \approx 2.6 \times 10^{-1}\ \text{m/sec}^{2}.$$

An additional consequence of the multilayer compensation-field architecture is the possibility of scaling the system toward substantially smaller propulsion platforms. In the present framework, the dominant fraction of the total energy budget is associated with the central field-generation core. Reducing the overall geometric scale of the structure correspondingly decreases the required active field volume and the associated stabilization power demand.

At smaller platform dimensions, a larger fraction of the total available energy can therefore be redirected from field maintenance toward propulsion dynamics and controlled spacetime-gradient modulation. Under optimistic but physically constrained scaling assumptions, the combined power requirements of the propulsion, stabilization, and optical confinement subsystems may potentially approach the order of 10^{9} W, comparable to the useful power output of a single modern nuclear reactor.

Although these estimates remain speculative and depend on idealized coherence and confinement conditions, the analysis suggests that multilayer coherent-field configurations may significantly improve the energetic scalability of structured vacuum-engineering systems.

Further work is required to refine the physical model, quantify energy requirements, and evaluate the feasibility of implementing such systems under realistic conditions. In particular, the integration of quantum-scale effects with macroscopic engineering constraints remains a key challenge for future research.

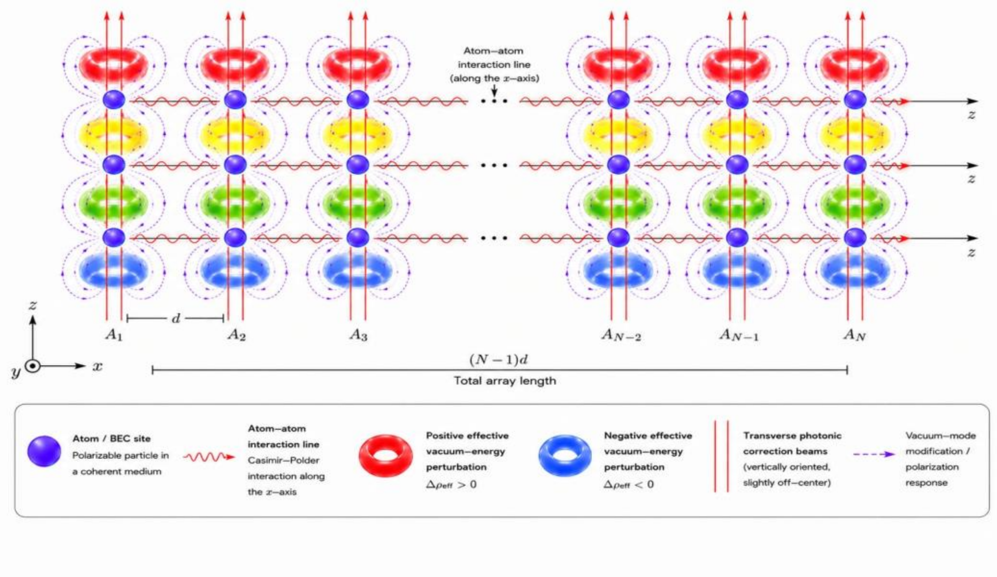

Figure 9. Conceptual multilayer configuration of coupled interaction regions in a structured ultracold platform.

An important direction for future research is the investigation of multilayer structured configurations in which overlapping interaction regions may generate cumulative modifications of effective photonic boundary conditions. Such effects could potentially lead to enhanced asymmetry of the effective vacuum-energy distribution across the BEC chamber.

Additional investigation is required to evaluate the influence of transverse photonic correction fields oriented perpendicular to the primary interaction axis (Figure 9). In particular, it remains unclear how such fields may affect the anisotropy, coherence stability, and effective vacuum-mode structure of multilayer coupled configurations.

It may also be useful to investigate the introduction of auxiliary weak blue-detuned correction fields for fine perturbative control of the structured interaction environment. Unlike the primary far red-detuned trapping fields, such auxiliary fields would not be required to provide the dominant gravitational confinement of the atomic ensembles. Although blue-detuned configurations generally introduce higher scattering and noise levels than strongly detuned 10.6 μm trapping fields, their contribution to decoherence and quantum noise may remain limited at sufficiently low optical power.

In distributed multilayer configurations, auxiliary correction fields may only need to be applied locally to selected trapping regions. If partial coherent coupling between neighboring structured interaction zones is preserved, local perturbative adjustments could potentially influence the collective configuration of the surrounding photonic and ultracold environment.

Nevertheless, the proposed framework may serve as a foundation for future investigations into controlled field configurations and their potential applications in advanced propulsion concepts.

* Conceptual visualizations in Figures 1–3 and 9 were prepared with AI-assisted graphical support.

** The author's technical background includes practical experience with fiber-optic communication systems and optical signal infrastructure.

[1] C. W. Misner, K. S. Thorne, and J. A. Wheeler, Gravitation, W. H. Freeman and Company, San Francisco (1973), ISBN: 978-0-7167-0344-0;

[2] S. Weinberg, Gravitation and Cosmology: Principles and Applications of the General Theory of Relativity, John Wiley & Sons, New York (1972), ISBN: 978-0-471-92567-5;

[3] Hartle, J. B. Gravity: An Introduction to Einstein's General Relativity, San Francisco: Addison-Wesley (2003), ISBN: 978-0805386622;

[4] R. C. Tolman, P. Ehrenfest, and B. Podolsky, On the Gravitational Field Produced by Light, Physical Review, Vol. 37, No. 5, (1931), DOI: 10.1103/PhysRev.37.602;

[5] W. B. Bonnor, The Gravitational Field of Light, Communications in Mathematical Physics, Vol. 13, No. 3, (1969), DOI: 10.1007/BF01645483;

[6] M. Alcubierre, The Warp Drive: Hyper-Fast Travel within General Relativity, Classical and Quantum Gravity, Vol. 11, No. 5, (1994), DOI: 10.1088/0264-9381/11/5/001;

[7] T. Y. Fan, Laser Beam Combining for High-Power, High-Radiance Sources, IEEE Journal of Selected Topics in Quantum Electronics, Vol. 11, No. 3, (2005), DOI: 10.1109/JSTQE.2005.850241;

[8] H. White, J. Vera, A. Han, A. R. Bruccoleri, and J. MacArthur, “Worldline Numerics Applied to Custom Casimir Geometry Generates Unanticipated Intersection with Alcubierre Warp Metric,” European Physical Journal C 81, 899 (2021), DOI: 10.1140/epjc/s10052-021-09781-3;

[9] J. Rui, D. Wei, A. Rubio-Abadal, S. Hollerith, J. Zeiher, D. M. Stamper-Kurn, C. Gross, and I. Bloch, “A Subradiant Optical Mirror Formed by a Single Structured Atomic Layer,” Nature 583, 369–374 (2020), DOI: 10.1038/s41586-020-2461-4;

[10] Casimir, H. B. G., and Polder, D. “The Influence of Retardation on the London–van der Waals Forces.” Physical Review 73(4), 360–372 (1948), DOI: 10.1103/PhysRev.73.360;

[11] M. Antezza, L. P. Pitaevskii and S. Stringari, Effect of the Casimir-Polder force on the collective oscillations of a trapped Bose-Einstein condensate, Physical Review A, Vol. 70, 053619 (2004), DOI: 10.1103/PhysRevA.70.053619;

[12] J. M. Obrecht, R. J. Wild, M. Antezza, L. P. Pitaevskii, S. Stringari and E. A. Cornell, Measurement of the Temperature Dependence of the Casimir-Polder Force, Physical Review Letters, Vol. 98, 063201 (2007), DOI: 10.1103/PhysRevLett.98.063201;

[13] Haroche, S., and Raimond, J.-M. Exploring the Quantum: Atoms, Cavities, and Photons. Oxford University Press, Oxford (2006), ISBN: 978-0198509141;

[14] I. Bloch, “Ultracold Quantum Gases in Optical Lattices,” Nature Physics 1(1), 23–30 (2005), DOI: 10.1038/nphys138;

[15] J. M. Wylie and J. E. Sipe, Quantum electrodynamics near an interface, Physical Review A, Vol. 30, No. 3, (1984), DOI: 10.1103/PhysRevA.30.1185;

[16] M. Bordag, G. L. Klimchitskaya, U. Mohideen, and V. M. Mostepanenko, Advances in the Casimir Effect, Oxford University Press, Oxford (2009), ISBN: 978-0-19-923874-3;

[17] H. Ritsch, P. Domokos, F. Brennecke, and T. Esslinger, "Cold Atoms in Cavity-Generated Dynamical Optical Potentials," Reviews of Modern Physics 85(2), 553–601 (2013), DOI: 10.1103/RevModPhys.85.553;

[18] F. Capasso, J. N. Munday, D. Iannuzzi, and H. B. Chan, Casimir Forces and Quantum Electrodynamical Torques: Physics and Nanomechanics, IEEE Journal of Selected Topics in Quantum Electronics, Vol. 13, No. 2, (2007), DOI: 10.1109/JSTQE.2007.893569;

[19] J. B. Pendry, D. Schurig, and D. R. Smith, Controlling Electromagnetic Fields, Science, Vol. 312, No. 5781, (2006), DOI: 10.1126/science.1125907;

[20] L. D. Landau and E. M. Lifshitz, The Classical Theory of Fields, 4th Edition, Butterworth-Heinemann, Oxford (1975). Course of Theoretical Physics, Vol. 2, ISBN: 978-0-7506-2768-9;

[21] E. M. Purcell, Life at Low Reynolds Number, American Journal of Physics, Vol. 45, No. 1, (1977), DOI: 10.1119/1.10903;

[22] A. H. Shapiro, M. Y. Jaffrin, and S. L. Weinberg, Peristaltic Pumping with Long Wavelengths at Low Reynolds Number, Journal of Fluid Mechanics, Vol. 37, No. 4, (1969), DOI: 10.1017/S0022112069000899;

[23] N. Ashby, "Relativity in the Global Positioning System," Living Reviews in Relativity 6, Article 1 (2003), DOI: 10.12942/lrr-2003-1;

[24] Ashby, N. "Relativity in the Global Positioning System." Living Reviews in Relativity 6, Article 1 (2003), DOI: 10.12942/lrr-2003-1;

[25] Takano, T., Takamoto, M., Ushijima, I., Ohmae, N., Akatsuka, T., Yamaguchi, A., Kuroishi, Y., Munekane, H., Miyahara, B., and Katori, H. "Geopotential Measurements with Synchronously Linked Optical Lattice Clocks." Nature Photonics 10(10), 662–666 (2016), DOI: 10.1038/nphoton.2016.159;

[26] Bloch, I., Dalibard, J., and Zwerger, W. "Many-Body Physics with Ultracold Gases." Reviews of Modern Physics 80(3), 885–964 (2008), DOI: 10.1103/RevModPhys.80.885;

[27] Fortágh, J., and Zimmermann, C. "Magnetic Microtraps for Ultracold Atoms." Reviews of Modern Physics 79(1), 235–289 (2007), DOI: 10.1103/RevModPhys.79.235;

[28] Bakr, W. S., Gillen, J. I., Peng, A., Fölling, S., and Greiner, M. "A Quantum Gas Microscope for Detecting Single Atoms in a Hubbard-Regime Optical Lattice." Nature 462, 74–77 (2009), DOI: 10.1038/nature08482;

[29] Sherson, J. F., Weitenberg, C., Endres, M., Cheneau, M., Bloch, I., and Kuhr, S. “Single-Atom-Resolved Fluorescence Imaging of an Atomic Mott Insulator.” Nature 467, 68–72 (2010), DOI: 10.1038/nature09378;

[30] Lamport L. The Part-Time Parliament. ACM Trans Comput Syst. (1998) 16(2):133–169, DOI: 10.1145/279227.279229;

[31] Ritsch, H., Domokos, P., Brennecke, F., and Esslinger, T. “Cold Atoms in Cavity-Generated Dynamical Optical Potentials.” Reviews of Modern Physics 85(2), 553–601 (2013), DOI: 10.1103/RevModPhys.85.553;

[32] Urvoy, A., Vendeiro, Z., Ramette, J., Adiyatullin, A., and Vuletić, V. “Direct Laser Cooling to Bose–Einstein Condensation in a Dipole Trap.” Physical Review Letters 122, 203202 (2019), DOI: 10.1103/PhysRevLett.122.203202;

[33] Gaunt, A. L., Schmidutz, T. F., Gotlibovych, I., Smith, R. P., and Hadzibabic, Z. “Bose–Einstein Condensation of Atoms in a Uniform Potential.” Physical Review Letters 110, 200406 (2013), DOI: 10.1103/PhysRevLett.110.200406;

[34] Ketterle, W., Durfee, D. S., and Stamper-Kurn, D. M. “Making, Probing and Understanding Bose–Einstein Condensates.” In: Proceedings of the International School of Physics ‘Enrico Fermi’, Course CXL, IOS Press (1999), arXiv:cond-mat/9904034;

[35] C. J. Pethick and H. Smith, Bose-Einstein Condensation in Dilute Gases, 2nd ed., Cambridge University Press (2008); ISBN: 978-0521846516;

[36] L. Pitaevskii and S. Stringari, Bose-Einstein Condensation, Oxford University Press (2003), ISBN: 978-0198507192;

[37] J. Fortagh and C. Zimmermann, Magnetic microtraps for ultracold atoms, Reviews of Modern Physics 79, (2007), DOI: 10.1103/RevModPhys.79.235;

[38] R. Grimm, M. Weidemüller and Y. B. Ovchinnicov, Optical Dipole Traps for Neutral Atoms, Advances in Atomic, Molecular, and Optical Physics, Vol. 42, (2000), DOI: 10.1016/S1049-250X(08)60186-X;

[39] Weber, T. Bose–Einstein Condensation of Optically Trapped Cesium. PhD Thesis, University of Innsbruck, Innsbruck, Austria (2003);

[40] T. F. Schmidutz, I. Gotlibovych, A. L. Gaunt, R. P. Smith and Z. Hadzibabic, Quantum Joule-Thomson effect in a saturated homogeneous Bose gas, Phys. Rev. Lett. 112, 040403 (2014), DOI: 10.1103/PhysRevLett.112.040403;

[41] Power, E. A., and Thirunamachandran, T. “Dispersion Forces Between Atoms with One or Both Atoms Excited.” Physical Review A 47(4), 2539–2546 (1993), DOI: 10.1103/PhysRevA.47.2539;

[42] S. Y. Buhmann, Dispersion Forces I, Springer Tracts in Modern Physics, Vol. 247, Springer (2012), DOI: 10.1007/978-3-642-32483-2;

[43] F. London, “Zur Theorie und Systematik der Molekularkräfte,” Zeitschrift für Physik 63, 245–279 (1930), DOI: 10.1007/BF01421741;

[44] V. A. Parsegian, Van der Waals Forces: A Handbook for Biologists, Chemists, Engineers, and Physicists, Cambridge University Press, Cambridge (2006), ISBN: 978-0521839068;

[45] B. E. A. Saleh and M. C. Teich, Fundamentals of Photonics, 2nd ed., Wiley-Interscience, Hoboken, NJ (2007), ISBN: 978-0471358329;

[46] Hung, C.-L., Zhang, X., Gemelke, N., and Chin, C. “Accelerating Evaporative Cooling of Atoms into Bose–Einstein Condensation in Optical Traps.” Physical Review A 78, 011604(R) (2008), DOI: 10.1103/PhysRevA.78.011604;

[47] Yariv, A. (1989). Quantum Electronics (3rd ed.). Wiley. Chapter 7.3: Phase accumulation and cavity modes, ISBN: 978-0-471-60997-5;

[48] P. W. Milonni and J. H. Eberly, Laser Physics, Wiley, Hoboken, NJ (2010), ISBN: 978-0-470-38551-1;

[49] D. Rychtarik, B. Engeser, H.-C. Nägerl, and R. Grimm, “Two-dimensional Bose-Einstein condensate in an optical surface trap,” Physical Review Letters 92, 173003 (2004), DOI: 10.1103/PhysRevLett.92.173003;

[50] Joannopoulos, J. D., Johnson, S. G., Winn, J. N., and Meade, R. D. Photonic Crystals: Molding the Flow of Light, 2nd Edition. Princeton University Press, Princeton, NJ (2008), ISBN: 978-0691124568;

[51] A. P. Goutzoulis and D. R. Pape, Design and Fabrication of Acousto-Optic Devices, Marcel Dekker, New York (1994), ISBN: 978-0824792237;

[52] J. E. Curtis, B. A. Koss, and D. G. Grier, “Dynamic holographic optical tweezers,” Optics Communications 207(1–6), (2002), DOI: 10.1016/S0030-4018(02)01524-9;

[53] D. A. B. Miller, “Are optical transistors the logical next step?”, Nature Photonics 4, 3–5 (2010), DOI: 10.1038/nphoton.2009.240;

[54] C. N. Danson, D. Hillier, N. Hopps, and D. Neely, “Petawatt and Exawatt Class Lasers Worldwide,” High Power Laser Science and Engineering 7, e54 (2019), DOI: 10.1017/hpl.2019.36;

[55] G. P. Agrawal, Nonlinear Fiber Optics, 5th Edition, Academic Press (2013), ISBN: 978-0123970237;

[56] S. M. Carroll, “The Cosmological Constant,” Living Reviews in Relativity 4, 1 (2001), DOI: 10.12942/lrr-2001-1;

[57] Inman, D. J. Engineering Vibration, 4th Edition. Pearson Education, Boston (2014), ISBN: 978-0132871693;

[58] Burgess, C. P. Introduction to Effective Field Theory: Thinking Effectively about Hierarchies of Scale. Cambridge University Press, Cambridge (2020), ISBN: 978-1108489423.